Chapter 2
Bulk Properties of Nuclei

Abstract Their sizes and masses are the most fundamental properties of nuclei. They have simple mass number dependences which suggest that the nucleus behaves like a liquid and lead to the liquid-drop model for the nucleus. In this chapter we learn these bulk properties of nuclei and their applications to discussing nuclear stability, muon-catalysed fusion and the structure of heavy stars. As an example of the applications we discuss somewhat in detail the basic features of fission and nuclear reactors. We also mention deviations from what are expected from the liquid-drop model which suggest the pairing correlation and shell effects. We also discuss the velocity and the density distributions of nucleons inside a nucleus.

2.1 Nuclear Sizes

2.1.1 Rutherford Scattering

At the beginning of the twentieth century when quantum mechanics was born, various models were proposed for the structure of atoms such as the *plum pudding* or *raisin bread model* of J.J. Thompson, which assumes that the plus charge distributes over whole atom together with electrons, and the *Saturn model* by Hantaro Nagaoka. Rutherford led these debates to conclusion through the study of scattering of alpha particles on atom. He proposed the existence of a central part of the atom, i.e., the core part, which bears all the positive charge that cancels out the total negative charge of electrons and also carries the dominant part of the mass of the atom. Rutherford named this core part nucleus, and gave the limiting value to its size.[1] At that time, Rutherford had been engaged in the detailed studies of the properties of alpha particles emitted from radioactive materials, and knew that the alpha particle is the ionized He. What Rutherford remarked in the experimental results of Marsden is that alpha

[1]It was 1911 when Rutherford submitted his article on the atomic model to a science journal. The idea and the formula of Rutherford were derived by stimulation of experimental results of his coworker Marsden who had been engaged in the study of scattering of alpha particles emitted from natural radioactive elements on matter. Furthermore, they have been confirmed experimentally to be correct by his collaborators Geiger and Marsden.

© Springer Japan 2017

N. Takigawa and K. Washiyama, *Fundamentals of Nuclear Physics*,
DOI 10.1007/978-4-431-55378-6_2

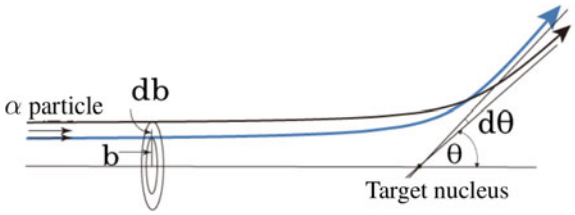


Fig. 2.1 Connection between the classical orbits of the Rutherford scattering and differential cross section

particles passing through matter sometimes make a large angle scattering, although most of them go nearly straight. This experimental feature cannot be explained by the Thompson model which assumes that positive charges distribute over the whole atom.[2]

It is established today that alpha particle is the nucleus of He. Here, we learn how the Rutherford model for atom was born, and how the information on the nuclear size is obtained through the scattering experiments of alpha particles.

Let us now consider the scattering of two structureless charged particles by Coulomb interaction, which is called Coulomb scattering or Rutherford scattering. Here, the two charged particles represent the alpha particle and the nucleus of the target atom. Since the mass of electrons is extremely small, one can ignore the scattering by electrons. The correct expression of the differential cross section for the Coulomb scattering can be obtained by classical mechanics, although, correctly speaking, one should use quantum mechanics. One important thing in this connection is that one to one correspondence holds between the impact parameter b and the scattering angle θ as illustrated in Fig. 2.1. The alpha particles which pass the area $2\pi b\mathrm{d}b$ of the impact parameter between b and $b + \mathrm{d}b$ in Fig. 2.1 are scattered to the region of solid angle $\mathrm{d}\Omega = 2\pi \sin\theta d\theta$ around the scattering angle θ. On the other hand, the differential cross section is defined as the number of particles scattered to the region of solid angle $\mathrm{d}\Omega$ when there exists one incident particle per unit time and unit area. Hence by definition

$$\frac{\mathrm{d}\sigma}{\mathrm{d}\theta} = \frac{2\pi b}{|\mathrm{d}\theta/\mathrm{d}b|}\,. \tag{2.1}$$

Using the relation

$$b = a\cot\left(\frac{\theta}{2}\right) \tag{2.2}$$

with

$$a = \frac{Z_1 Z_2 e^2}{\mu v^2} \tag{2.3}$$

[2]The history of the progress and discoveries of modern physics in the period from late in the nineteenth century to the beginning of the twentieth century is vividly described in the book by E. Segré [1].

which holds between the impact parameter b and the scattering angle θ in the case of Coulomb scattering, we obtain

$$\frac{\mathrm{d}\sigma}{\mathrm{d}\Omega} = \frac{\mathrm{d}\sigma_{\mathrm{R}}}{\mathrm{d}\Omega} \equiv \frac{1}{2\pi \sin\theta} \frac{\mathrm{d}\sigma}{\mathrm{d}\theta} = \frac{a^2}{4} \frac{1}{\sin^4(\theta/2)}, \tag{2.4}$$

where the index R in σ_{R} means the Rutherford scattering. In Eq. (2.3), μ is the reduced mass, and v is the speed of the relative motion in the asymptotic region, i.e., at the beginning of scattering. Note that Eq. (2.4) exactly agrees with the formula of the differential cross section $\mathrm{d}\sigma_{\mathrm{R}}/\mathrm{d}\Omega$ obtained quantum mechanically for the Rutherford scattering. The characteristics of the Coulomb scattering given by Eq. (2.4) are that the forward scattering is strong, but also that backward scattering takes place with a certain probability as well. These match the experimental results of Marsden.

The ground state of the natural radioactive nucleus $^{210}_{84}\mathrm{Po}$ decays with the half-life of 138.4 days by emitting an alpha particle ($^{210}_{84}\mathrm{Po} \rightarrow {}^{206}_{82}\mathrm{Pb} + \alpha$). The kinetic energy of the alpha particle is about 5.3 MeV corresponding to the Q-value of the decay 5.4 MeV. The differential cross section for the scattering, where this α particle is used to bombard the Au target of atomic number 79, agrees with that for the Rutherford scattering right up to the backward angle $\theta = \pi$. This suggests that the sum of the radii of Au and α ($R(\mathrm{Au}) + R(\alpha)$) is smaller than the distance of closest approach $d(\theta = \pi)$ for the scattering with the impact parameter $b = 0$ leading to the backward scattering $\theta = 180^\circ$ in the case of Rutherford scattering. Since the distance of closest approach d and the scattering angle θ or the impact parameter b is related by

$$d = a\left[1 + \csc\left(\frac{\theta}{2}\right)\right] = a + \sqrt{a^2 + b^2} \tag{2.5}$$

for the Rutherford scattering, the above mentioned experimental results give the upper boundary of the radius as $R(\mathrm{Au}) + R(\alpha) < 4.3 \times 10^{-12}$ cm. This upper boundary is much smaller than the radii of atoms, which are of the order of 10^{-8} cm. Rutherford was thus guided to his atomic model.

Figure 2.2 shows the ratio of the experimental differential cross section for the scattering of α particles of 48.2 MeV by Pb target to that for the corresponding Rutherford scattering $\mathrm{d}\sigma_{\mathrm{R}}/\mathrm{d}\Omega$ as a function of the scattering angle. The experimental cross section gets rapidly smaller than that of the Rutherford scattering beyond $\theta = 30^\circ$. This can be understood as the consequence of that the distance of closest approach is small for the scattering corresponding to large angle scattering as Eq. (2.5) shows, and hence the overlap between α particle and Pb becomes large, and consequently, those phenomena such as inelastic scattering which are excluded in the Rutherford scattering take place. Figure 2.3 shows classical trajectories obtained by fixing Pb at the origin and by making the incident energy of α particles to 48.2 MeV so as to match with Fig. 2.2. The circle shows the region corresponding to the sum of the radii of Pb and α particle, i.e., about 9.1 fm. The figure confirms that the distance of closest approach for the trajectories corresponding to large angle scattering becomes indeed smaller than the sum of the radii of Pb and α particle.

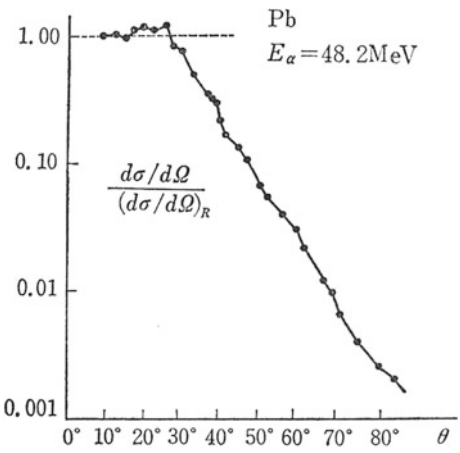


Fig. 2.2 Differential cross section of the elastic scattering of α particles by Pb. Taken from [2]

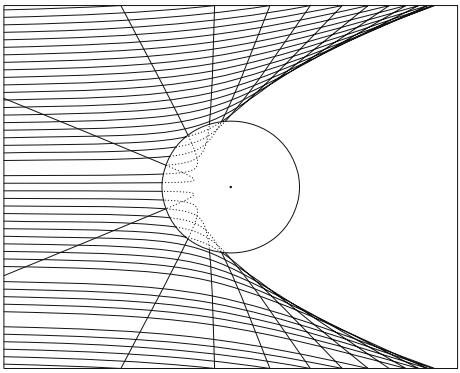


Fig. 2.3 Trajectories of Rutherford scattering

Exercise 2.1 Estimate the sum of the radii of α and Pb from the result of Fig. 2.2 based on the idea mentioned above.

The ratio of the differential cross section shown in Fig. 2.2 resembles the Fresnel diffraction of classical optics. The Fresnel diffraction occurs in the case where the source of light is located in the vicinity of the object that causes diffraction, e.g., an absorber. The scattering of α particles by a nucleus with large atomic number behaves like a Fresnel scattering, because the large Coulomb repulsion strongly bends the trajectory and works to make the source of light effectively locate in the vicinity of the scatterer. It is also because the partial waves corresponding to small impact parameters whose distance of closest approach is small are removed from the elastic scattering due to, e.g., inelastic scattering. Concerning the elastic scattering, this plays effectively the same role as that of an absorber.

This picture holds when the Coulomb interaction dominates the scattering process. The strength of the Coulomb interaction increases in proportion to the product of the charges of the projectile and target nuclei. On the other hand, roughly speaking,

the strength of the nuclear interaction increases in proportion to the reduced mass $A_1A_2/(A_1 + A_2)$. Hence the refraction effect due to the nuclear interaction becomes non-negligible for the scattering by a target nucleus with small atomic number. In fact, a similar differential cross section appears not by diffraction effect, but by refraction effect. The interpretation and analysis then get complicated. Accordingly, one can safely estimate the nuclear size based on the consideration of the Coulomb trajectory together with the strong absorption due to inelastic scattering as described in the present section when the atomic number of the target nucleus is large.

2.1.2 Electron Scattering

The scattering of α particles by a nucleus had led to the Rutherford atomic model, and provided a way to estimate the nuclear size. It thus played an important historical role. However, as stated at the end of the last section, it has a limitation regarding applicability. In contrast, the scattering of electrons by a nucleus, which we learn in this section, is a powerful method to study the nuclear size, more exactly, the distribution of protons inside a nucleus, because only well understood electromagnetic force is involved.[3,4]

2.1.2.1 The de Broglie Wavelength of Electron

In the experiments of electron scattering, electrons are injected on the target nucleus after they are accelerated by, e.g., a linear accelerator. In order to deduce the information on the nuclear size from electron scattering, the de Broglie wavelength of the electron must be of the same order of magnitude as that of the nuclear size or smaller. In this connection, let us first study the relation between the de Broglie wavelength of electron and the kinetic energy of electron supplied by the accelerator.

The de Broglie wavelength of electron λ_e is given by

$$\lambda_e = \frac{h}{p_e} \tag{2.6}$$

in terms of the momentum of the electron p_e and the Planck constant h. On the other hand, it holds that

$$E_{\text{total}} = \sqrt{m_e^2c^4 + p_e^2c^2} = m_ec^2 + E_{\text{kin}} = m_ec^2 + E_e \tag{2.7}$$

[3] R. Hofstadter was awarded the Nobel Prize in Physics 1961 for the study of high energy electron scattering with linear accelerator and the discovery of the structure of nucleon. He performed also systematic studies of nuclei by electron scattering.

[4] The electron scattering is a powerful method to learn the structure of nucleons mentioned in Chap. 1, and also to study nuclear excitations such as *giant resonances* and hypernuclei as well.

Table 2.1 The de Broglie wavelength of electron for some representative acceleration energies

Acceleration energy E_e (MeV)	100	200	300	1000	4000
de Broglie wavelength λ_e (fm)	12.4	6.2	4.1	1.2	0.31

by using the relation of relativity between the momentum and the energy of an electron, since the total energy of electron is given by adding the energy E_e supplied by the accelerator, i.e., the kinetic energy E_{kin}, to the rest energy. Hence,

$$p_e^2 = 2m_e E_e + E_e^2/c^2 \,. \tag{2.8}$$

By inserting Eq. (2.8) into (2.6), we obtain

$$\frac{\lambda_e}{2\pi} = \frac{\hbar c}{E_e(1 + 2m_e c^2/E_e)^{1/2}} \approx \frac{\hbar c}{E_e} \approx \frac{200}{E_e/\mathrm{MeV}}\,\mathrm{fm}\,. \tag{2.9}$$

We ignored the rest energy of electron $m_e c^2$ in the third and fourth terms of Eq. (2.9) by assuming that it is much smaller than the acceleration energy E_e. We have given not the wavelength itself, but the quantity which is obtained by dividing the wavelength by 2π to facilitate the estimate of the order of magnitude.

Table 2.1 gives the de Broglie wavelength of electron estimated by Eq. (2.9) for some representative acceleration energies.

2.1.2.2 Form Factor

As Table 2.1 shows, one has to inject electrons on a nucleus after having accelerated them to much higher energy than the rest energy of electron $m_e c^2 \approx 0.51\,\mathrm{MeV}$ in order to learn the nuclear size, which is of the order of fm. Hence one needs to use the Dirac equation, to which a relativistic Fermi particle obeys, in order to theoretically derive the proper expression of the differential cross section [3].

Exercise 2.2 Evaluate the ratio v/c of the velocity of the electron v to the speed of light in the vacuum c when the acceleration energy of the electron E_e is 100 MeV.

However, here let us simplify the problem in the following way, and learn how the information on nuclei can be obtained from the analyses of the electron scattering:

1. Treat the scattering of electrons by the electromagnetic field made by a nucleus, instead of considering the scattering of electrons by the nucleons inside the nucleus.
2. Consider only the Coulomb force (electric force) and ignore the magnetic force.
3. Use non-relativistic Schrödinger equation.

We express the Coulomb potential as $V(\mathbf{r})$. The scattering amplitude to the angle θ is then given by

$$f^{(1)}(\theta) = -\frac{1}{4\pi}\frac{2\mu}{\hbar^2}\int \mathrm{e}^{-\mathrm{i}\mathbf{q}\cdot\mathbf{r}} V(\mathbf{r})\mathrm{d}\mathbf{r} \tag{2.10}$$

following the first order Born approximation, which is valid because of the high energy scattering, and also because the involved electric force is weak compared to the kinetic energy. The μ is the reduced mass. It can be identified with the mass of electron m_e to a high degree of accuracy. The $\mathbf{q}$ is the momentum transfer divided by $\hbar$ and is given by

$$\mathbf{q} = \mathbf{k}_\mathrm{f} - \mathbf{k}_\mathrm{i}\,, \tag{2.11}$$

$$q = |\mathbf{q}| = 2k\sin(\theta/2)\,. \tag{2.12}$$

where $\mathbf{k}_\mathrm{i}$ is the wave-vector of the incident electron, $\mathbf{k}_\mathrm{f}$ is the wave-vector of the electron scattered to the direction of angle θ and k is the wave number of the electron corresponding to the incident energy.

Exercise 2.3 Derive Eqs. (2.10)–(2.12).

We remark that the potential $V(\mathbf{r})$ obeys the following Poisson equation,

$$\Delta V = 4\pi Ze^2\rho_C(\mathbf{r})\,, \tag{2.13}$$

in order to relate the scattering amplitude to the distribution of protons inside a nucleus. The Z is the atomic number of the nucleus to be studied, and $\rho_C(\mathbf{r})$ is the charge density at the position $\mathbf{r}$ measured from the center of the nucleus.[5] It is normalized as

$$\int \rho_C(\mathbf{r})\mathrm{d}\mathbf{r} = 1\,. \tag{2.14}$$

By repeating the integration by parts twice in Eq. (2.10), and by using Eq. (2.13), we obtain,

$$f^{(1)}(\theta) = \frac{Ze^2}{2\mu v^2}\frac{1}{\sin^2(\theta/2)}F(\mathbf{q})\,, \tag{2.15}$$

where $F(\mathbf{q})$ is defined as

$$F(\mathbf{q}) \equiv \int \mathrm{e}^{-\mathrm{i}\mathbf{q}\cdot\mathbf{r}}\rho_C(\mathbf{r})\mathrm{d}\mathbf{r}\,. \tag{2.16}$$

The differential cross section is therefore given by

$$\frac{d\sigma^{(1)}}{d\Omega} = |f^{(1)}(\theta)|^2 = \frac{d\sigma_\mathrm{R}}{d\Omega}|F(\mathbf{q})|^2\,. \tag{2.17}$$

[5] The distribution of protons ρ_p can be derived from ρ_C by taking into account the intrinsic structure of proton.

Correctly, the expression of the differential cross section is obtained as

$$\frac{\mathrm{d}\sigma^{(1)}}{\mathrm{d}\Omega} = \frac{\mathrm{d}\sigma_{\mathrm{M}}}{\mathrm{d}\Omega}|F(\mathbf{q})|^2 , \tag{2.18}$$

$$\frac{\mathrm{d}\sigma_{\mathrm{M}}}{\mathrm{d}\Omega} = \left[\frac{Ze^2}{2E_{\mathrm{e}}\sin^2(\theta/2)}\right]^2 \left[1 - \frac{v^2}{c^2}\sin^2(\theta/2)\right]$$

$$\approx \left[\frac{Ze^2\cos(\theta/2)}{2E_{\mathrm{e}}\sin^2(\theta/2)}\right]^2 , \tag{2.19}$$

by replacing the differential cross section of the Rutherford scattering $\mathrm{d}\sigma_{\mathrm{R}}/\mathrm{d}\Omega$ by that for the Mott scattering $\mathrm{d}\sigma_{\mathrm{M}}/\mathrm{d}\Omega$ which takes into account relativistic effects for electrons. The $\mathrm{d}\sigma_{\mathrm{M}}/\mathrm{d}\Omega$ gives the differential cross section of the scattering of electrons by the Coulomb force made by a point charge. Equation (2.18) shows that the information on the density distribution of protons inside a nucleus can be obtained through the ratio of the experimental differential cross section to that for the Mott scattering. The $F(\mathbf{q})$ defined by Eq. (2.16) is the factor which represents the effects of the finiteness of the nuclear size and is called the *form factor*.

Especially, if the nucleus is spherical, i.e., if the charge distribution is spherical, the form factor is given by

$$F(q) = 4\pi \int_0^\infty \rho_C(r) j_0(qr) r^2 \mathrm{d}r = 4\pi \int_0^\infty \rho_C(r) \frac{\sin(qr)}{qr} r^2 \mathrm{d}r , \tag{2.20}$$

where $j_0(x)$ is the spherical Bessel function of the first kind.

Exercise 2.4 Prove Eq. (2.20) in the following two methods:

1. Perform directly the integration over the angular part of $\mathbf{r}$ ($\mathrm{d}\Omega_r$) in Eq. (2.16).
2. Expand at first the $\mathrm{e}^{-\mathrm{i}\mathbf{q}\cdot\mathbf{r}}$ in terms of Legendre functions, and then use the orthonormal property of the spherical harmonics.

2.1.2.3 Density Distribution

(1) Estimate of the Nuclear Radius from Diffraction Pattern As Table 2.1 implies, the experiments of electron scattering are performed with high energy in order to study nuclear size and the density distribution of protons inside a nucleus. The corresponding differential cross section is expected to show a diffraction pattern similar to that of the Fraunhofer diffraction in optics. Figure 2.4 shows the differential cross section for the elastic scattering of electrons from Au target at 153 and 183 MeV. The monotonically decreasing solid line is the Mott scattering cross section for 183 MeV. The figure shows that the observed cross section is smaller than that for the Mott scattering, and that it has indeed the diffraction pattern, i.e., oscillation, of the Fraunhofer type.

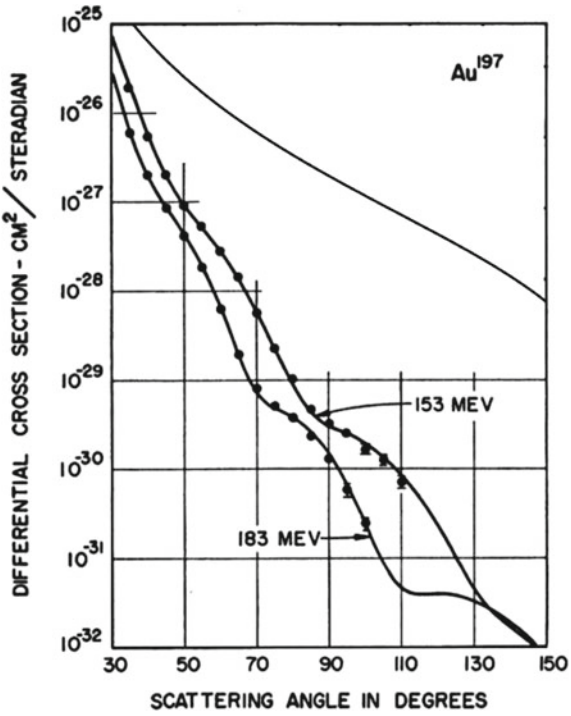


Fig. 2.4 The elastic electron-scattering differential cross section from Au at energies of 153 and 183 MeV. Taken from [4]

Let us assume that the charge distributes uniformly inside a nucleus with a spherical shape of radius R in order to see how the nuclear size is estimated from the diffraction pattern. The resulting form factor reads

$$F(q) = \frac{3}{qR} j_1(qR) = \frac{3}{qR}(qR)^{-2}[\sin(qR) - (qR)\cos(qR)]\,. \tag{2.21}$$

We then find that the zeros of $j_1(x)/x$ correspond to the angles where the differential cross section shows local minima. We denote the magnitude of the transferred momenta corresponding to those scattering angles $\theta_1, \theta_2, \ldots$ by $q_1, q_2, \ldots$. The first zero of $j_1(x)/x$ is $x_1 \approx 4.49$, and the interval between the successive zeros Δx is about π afterwards. One can therefore estimate the radius either by $R \sim x_1/q_1$ or by $R \sim \pi/(q_2 - q_1)$ using the $q_1, q_2, \ldots$ evaluated from $\theta_1, \theta_2, \ldots$, which are extracted from the experimental data.

Exercise 2.5 Estimate the radius of the nucleus of Au from the experimental data shown in Fig. 2.4.[6]

[6]The dips in diffraction pattern are buried by the distortion effects due to Coulomb force in the case of target nuclei with a large mass number such as Au. The diffraction pattern appears more clearly for the target nuclei with small mass number.

(2) The Woods–Saxon Representation of the Density Distribution Accurate information on the density distribution[7] of nucleons inside a nucleus can be obtained by making the Fourier transformation of the form factor given by the experiments of electron scattering. However, one usually takes the method to first postulate a plausible functional form, then determine the parameters therein to reproduce the experimental data. In that case, a widely adopted choice is to assume the following functional form called the *Woods–Saxon type*,[8]

$$\rho(r) = \frac{\rho_0}{1 + \mathrm{e}^{(r-R)/a}}\,, \tag{2.22}$$

where R is the parameter to represent the radius. a is the parameter to represent the thickness of the surface area and is called the surface diffuseness parameter. The density falls from 90 to 10% of the central density over the region of thickness of 4.4 times a around R. The ρ_0 is the central density, and is given as a function of R and a through the normalization condition,

$$\int \rho \mathrm{d}\mathbf{r} \sim \rho_0 \frac{4\pi}{3} R^3 \left[1 + \pi^2 \left(\frac{a}{R}\right)^2\right] = A\,. \tag{2.23}$$

The two solid curves in Fig. 2.4 which reproduce fairly well the experimental differential cross section have been calculated with the best fit parameters for the data at 183 MeV by assuming the Woods–Saxon representation for the charge distribution.

The following values are obtained from the analyses of experimental data for a large number of stable target nuclei,

$$R \sim (1.1\text{–}1.2) A^{1/3}\,\mathrm{fm}\,, \quad a \sim 0.6\,\mathrm{fm}\,, \quad \rho_0 \sim (0.14\text{–}0.17)\,\mathrm{fm}^{-3}\,, \tag{2.24}$$

as parameters in the Woods–Saxon parametrization.[9] The fact that the radius is proportional to the 1/3 power of the mass number, i.e., the number of nucleons composing the nucleus, and that the density is independent of the mass number

[7] In stable nuclei, the protons and neutrons distribute inside the nucleus almost in the same way. Here, we therefore treat the density distribution of protons and of nucleons as the same except for the absolute value. In these days, extensive studies are performed on the nuclei far from the β-stability line, which are called unstable nuclei. It is then getting known that some of them have very different distributions for protons and for neutrons. For example, the region where there exists only neutrons largely extends over the surface region in some nuclei such as ^{11}Li in the vicinity of the neutron drip line. Such layer is called the *neutron halo*. Recently, it is reported from the inelastic scattering of polarized protons (see [5]) and also from the elastic scattering of polarized electrons that even a typical stable nucleus ^{208}Pb has a larger radius of the neutron distribution than that of the proton distribution by 0.15–0.33 fm. Relatedly, the study of the existence of the region consisting of only neutrons, which is called *neutron skin*, is an active area of research.

[8] There exist deviations from the Woods–Saxon type for individual nucleus. They are explained by shell model.

[9] The value $\rho_0 \sim 0.17\,\mathrm{fm}^{-3}$ is widely accepted as the density of nuclear matter (see [6] for the argument about the detailed mass number dependence of the central density of nuclei with large mass number).

suggest that the nucleus has a property as a *liquid*.[10] The fact that the density is independent of the mass number is called the *saturation property of nuclear density*.

Incidentally, the surface area dominates in light nuclei. The *Gaussian type* is therefore often used, instead of the Woods–Saxon type, as a more realistic functional form.

2.1.2.4 The Root-Mean-Square Radius

The radius of a nucleus is the average of the radii of the region of spatial occupation of the nucleons composing the nucleus. Hence the concept of root-mean-square radius is often used in discussing nuclear size. We first define the mean-square radius by

$$\langle r^2 \rangle \equiv \int_0^\infty r^2 \rho(r) 4\pi r^2 \mathrm{d}r \Big/ \int_0^\infty \rho(r) 4\pi r^2 \mathrm{d}r \,. \tag{2.25}$$

The root-mean-square radius $R_{\mathrm{r.m.s.}}$ is then defined by taking the square root as $R_{\mathrm{r.m.s.}} \equiv \sqrt{\langle r^2 \rangle}$.

We assumed a sharp density distribution without a surface diffuseness, i.e., a step function, in a simple analysis of the diffraction pattern of the electron scattering, e.g., as shown in Eq. (2.21). We name the resulting radius the *equivalent radius* or the *effective sharp radius* and designate it as R_{eq}. By definition, $R_{\mathrm{r.m.s.}}$ and R_{eq} are related to each other as

$$R_{\mathrm{eq}} = \sqrt{\frac{5}{3}\langle r^2 \rangle} = \sqrt{\frac{5}{3}} R_{\mathrm{r.m.s.}} \,. \tag{2.26}$$

Since R_{eq} is proportional to the $1/3$ power of the mass number A, let us represent it as

$$R_{\mathrm{eq}} = r_0 A^{1/3} \,. \tag{2.27}$$

The proportional coefficient r_0, called *radius parameter*, is then independent of individual nucleus, and takes experimentally the value[11] of

$$r_0 \sim 1.1\text{–}1.2 \text{ fm} \,. \tag{2.28}$$

---

[10] Although the nucleus appears like a drop of liquid, it is not a classical liquid, but a drop of *quantum liquid*, since commutation relations govern the nucleus. In the classical liquid, the momentum space is not deformed even if it is spatially deformed. On the other hand, in the case of nuclei, a spatial deformation leads to the deformation in the momentum space through the uncertainty relation (see the footnote concerning quantum liquid in Sect. 8.3.4).

[11] Equations (2.24), (2.27) and (2.28) hold for stable nuclei. It has been found that the radii of unstable nuclei, especially of nuclei in the vicinity of neutron drip line, significantly deviate from these equations. For example, in the case of Li isotopes, the radius of ^{11}Li which has a neutron halo as mentioned before and thus called a halo nucleus or a neutron halo nucleus is much larger than what we expect from Eq. (2.27), although the radii of stable isotopes ^{6,7}Li and of the isotopes ^{8,9}Li which lie close to the stability line vary with A almost following Eq. (2.27).

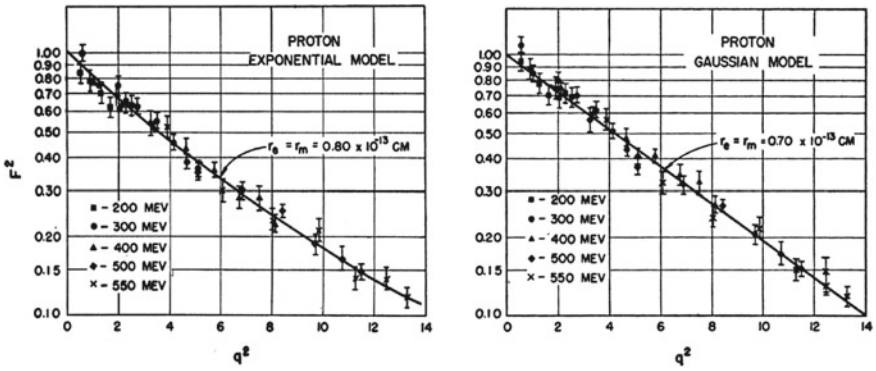


Fig. 2.5 The form factor of the electron scattering by proton. Taken from [7]

If we assume the density distribution of the Woods–Saxon type given by Eq. (2.22), Eq. (2.26) is replaced by

$$\langle r^n \rangle \equiv \frac{\int r^n \rho(r) \mathrm{d}\mathbf{r}}{\int \rho(r) \mathrm{d}\mathbf{r}} = \frac{3}{n+3} R^n \left[1 + \frac{n(n+5)}{6} \pi^2 \left(\frac{a}{R} \right)^2 + \cdots \right] . \tag{2.29}$$

From Eqs. (2.16) and (2.25), we obtain

$$\begin{aligned} F(q) &= 1 - \frac{1}{3!} \langle r^2 \rangle q^2 + \cdots , \\ |F(q)|^2 &= 1 - \frac{1}{3} \langle r^2 \rangle q^2 + \cdots , \end{aligned} \tag{2.30}$$

for small values of the momentum transfer. These formulae show that the nuclear size can be estimated by studying the form factor for the forward scattering or the behaviour of the form factor in the region of small momentum transfer. Figure 2.5 shows a similar analysis for the radius of proton. It is derived from the analysis of this experimental data that the root-mean-square radius of proton $R_{\mathrm{r.m.s.}}$ is 0.7–0.8 fm.[12, 13]

[12] The measurement with high accuracy in the extreme forward region, where q^2 is extremely small, is a difficult task and is a challenging subject in these days. In practice, one estimates the radius by analysing the data in the region where the measurement with high accuracy is doable, by assuming, e.g., the exponential or the Gaussian density distribution as shown in Fig. 2.5. Also, it is known that it is necessary to take into account the magnetic effects for the case of nucleons.

[13] As Fig. 2.5 shows, the experimental data for the region of small momentum transfer can be reproduced equally well by assuming the charge distribution in a proton to be either exponential or Gaussian type. Historically, the charge distribution of exponential type has been considered to be a good approximation, and correspondingly, the form factor of dipole type has been used. However, it is getting known from recent studies that the experimental data significantly deviate from the form factor of the dipole type, and it is argued that the charge distribution inside a proton is closer to a Gaussian type.

Exercise 2.6 The radius of the charge distribution of a nucleus can be estimated also from the energy spectrum of the X-ray of the corresponding muonic-atom, or the energy difference between the corresponding energy levels of mirror nuclei.[14] Study the principle of each method.

2.1.3 Mass Distribution

All the methods mentioned above are the method to study the distribution of protons, in other words, the *charge distribution* in nuclei, and give no information on the distribution of neutrons. One has to use other methods in order to study the distribution of nucleons including neutrons, which is often called the *mass distribution*, inside a nucleus. The scattering of protons or neutrons by a nucleus, where the strong interaction is involved, and nucleus-nucleus collisions are the examples. Similarly to the case of electron scattering, high incident energies are appropriate. Here we consider two methods.

2.1.3.1 High-Energy Neutron Scattering: Fraunhofer Scattering

Let us first consider the high-energy neutron scattering. Since the interaction between the neutron and the target nucleus is strong, neutrons are absorbed or the target nucleus is excited when the neutrons reach the area of the target nucleus. The associated cross section, i.e., the sum of the cross sections of inelastic scattering and of absorption, is intuitively expected to be given by $\sigma^{(\text{inel})} \sim \pi R^2$ by using the nuclear radius R. On the other hand, in the scattering of relatively high energy by a short range interaction, the elastic scattering corresponds to the shadow scattering in quantum mechanics and the magnitude of its cross section is also expected to be the same, i.e., $\sigma^{(\text{el})} \sim \pi R^2$. In consequence, the total cross section is given by $\sigma^{(\text{total})} \sim 2\pi R^2$. One can therefore obtain the information on nuclear size by measuring the cross section of high-energy neutron scattering.

In order to make the arguments more precise, let us consider the partial wave analysis of neutron scattering by a nucleus, and postulate that the S-matrix of the elastic scattering of each partial wave ℓ is given by

$$S^{(\text{el})} = \begin{cases} 0 & \text{for } \ell \leq kR \\ 1 & \text{for } \ell > kR\,, \end{cases} \tag{2.31}$$

[14] The pair nuclei such as ${}^{15}_{7}\text{N}_8$ and ${}^{15}_{8}\text{O}_7$ which have interchanged numbers of protons and neutrons are called *mirror nuclei* to each other. Their energy levels are nearly equal, but shifted.

by emphasizing the above mentioned absorption effects and the characteristic of high-energy scattering that the phase shift is small. By inserting the extreme postulate Eq. (2.31) called the sharp-cut-off-model into the partial wave expansion formulae, Eqs. (A.6), (A.8) and (A.10), for the total cross sections of elastic scattering $\sigma^{(\mathrm{el})}$ and of inelastic scattering $\sigma^{(\mathrm{inel})}$ and for the total cross section $\sigma^{(\mathrm{total})} = \sigma^{(\mathrm{el})} + \sigma^{(\mathrm{inel})}$, or into their integral representations transformed to the form of Poisson sum formula (see Eq. (A.23)), we can confirm that $\sigma^{(\mathrm{el})} \sim \pi R^2$, $\sigma^{(\mathrm{inel})} \sim \pi R^2$, $\sigma^{(\mathrm{total})} \sim 2\pi R^2$.

Experimentally, the total scattering cross section $\sigma^{(\mathrm{total})}$ can be determined relatively easily by the *attenuation method*. In this method, the information on the cross section is obtained by comparing the counts, which are observed with detectors placed in the forward direction, in the measurements with and without scatterer. If we represent the former and the latter as I and I_0, respectively, then it holds that

$$\frac{I}{I_0} = \exp\left(-\sigma^{(\mathrm{total})} nt\right), \tag{2.32}$$

where n is the number density of the target nucleus inside the scatterer, and t the thickness of the scatterer.

Incidentally, the scattering where the S-matrix is given by Eq. (2.31) corresponds to the Fraunhofer diffraction in classical optics. A semi-classical scattering theory leads to the following concise analytic expression for the associated differential cross section of the elastic scattering,

$$\frac{\mathrm{d}\sigma}{\mathrm{d}\Omega} = R^2 \frac{1}{\theta \sin\theta} |J_1(kR\theta)|^2 . \tag{2.33}$$

The property of the Bessel function $J_1(x)$ suggests that the elastic scattering has large intensities at forward angles. This is nothing but the shadow scattering mentioned at the beginning of this section.

Another important thing is that an oscillatory diffraction pattern is observed. The interval between two successive angles, where the cross section takes local maxima, is given by $\Delta\theta_D \sim \pi/kR$ from the property of the Bessel function. Hence one can deduce a value for the nuclear size from the angular spacing of the diffraction pattern. The validity of the Fraunhofer diffraction method described in this section can be assessed by comparing thus obtained nuclear radius with the nuclear radius obtained from the measurement of the total cross section.

One can also use a high-energy proton–nucleus scattering to study the mass distribution. However, the simple model given by Eq. (2.31) cannot be applied in that case because of the long range Coulomb interaction. In fact, the cross section diverges in the Coulomb scattering. A special consideration is therefore required to handle the scattering by Coulomb interaction.

2.1.3.2 Analysis of High-Energy Nucleon–Nucleus and Nucleus–Nucleus Reaction Cross Sections by Glauber Theory

The high-energy potential scattering can be well described by the *eikonal approximation*, where the scattering phase shift is determined based on the assumption that the reaction takes place along a straight line trajectory. If one applies this idea to the nucleon–nucleus and nucleus–nucleus scatterings, and takes the folding model, where the potential in the eikonal approximation is approximated by folding interactions between either incident nucleon or incident nucleus and constituent nucleons in the target nucleus, then one obtains the following expressions

$$\sigma_R = 2\pi \int_0^\infty b\mathrm{d}b\,[1 - T(b)]\,, \tag{2.34}$$

$$T(b) = \exp(-\bar{\sigma}_{NN} O_v(b))\,, \tag{2.35}$$

$$O_v(b) = \int_{-\infty}^{\infty} \mathrm{d}z \int \mathrm{d}\mathbf{r} \rho_T(\mathbf{r}) \rho_P(\mathbf{r} - \mathbf{R})\,, \tag{2.36}$$

which give the total reaction cross section σ_R in terms of the total reaction cross section of the nucleon–nucleon scattering (see Appendix A.4.2). The $\bar{\sigma}_{NN}$ in the *transparency function* $T(b)$ is the average of the total cross section in the proton–neutron and proton–proton scatterings. If one denotes the collision energy in the nucleon–nucleon scattering by $E_{\mathrm{lab}}^{(NN)}$, that in the nucleus–nucleus scattering by $E_{\mathrm{lab}}^{(nn)}$, and the mass number of the projectile nucleus by A_P, then one should use the energy given by the relationship

$$E_{\mathrm{lab}}^{(NN)} = E_{\mathrm{lab}}^{(nn)} / A_P\,, \tag{2.37}$$

(the reasoning is given in Appendix A.4.2). The $O_v(b)$ is called the *overlap function*. It is given by integrating the overlap of the densities of the incident nucleus (or incident nucleon) and of the target nucleus for the impact parameter b over the collision direction (named z-direction) which is perpendicular to b. The $\mathbf{R} = (\mathbf{b}, z)$ is the relative coordinate between the projectile and target nuclei. Since the overlap integral clearly depends on the nuclear size and the distribution of nucleons inside nuclei, one can extract information on those quantities from the analysis of the reaction cross section based on Eq. (2.34).

Equations (2.34)–(2.37) are called the *optical limit formulae* of the Glauber theory, whose derivation is given in Appendix A.4.2. It is necessary to extend them either by taking into account higher order terms in the so-called cumulant expansion method or by using the *diffractive eikonal approximation* which goes beyond the optical limit approximation in order to correctly estimate the size and the reaction cross section of the nuclei in the vicinity of the drip line, whose studies are recently extensively going on, by analyzing their scattering data in terms of the Glauber theory (see, e.g., [8–10]).

2.2 Number Density and Fermi Momentum of Nucleons

2.2.1 Number Density of Nucleons

Let us denote the number density of nucleons inside a nucleus by ρ. Since ρ is defined as the mass number A divided by the volume V, we have

$$\rho \equiv \frac{A}{V} = \frac{3}{4\pi r_0^3} \tag{2.38}$$

from Eq. (2.27) for spherical nuclei. As Eq. (2.28) shows, the radius parameter r_0 is almost constant independently of the mass number. Equation (2.38) therefore shows that the number density of nucleons inside a nucleus is almost constant independently of individual nucleus. This property is called the *density saturation*, and is one of the experimental evidences of the liquid-like behaviour of nuclei leading to the *liquid-drop model of nucleus*.

2.2.2 Fermi Momentum: Fermi-Gas Model, Thomas–Fermi Approximation

One of the simple pictures for the nucleus as a many-body system of nucleons, which are fermions, is the so-called *Fermi-gas model* or *Thomas–Fermi approximation*. In that method, each nucleon is considered to be moving independently from each other in a mean field of volume V. However, the *Pauli exclusion principle* that each quantum state can be occupied by at most only one fermion is respected. Consequently, the nucleons become to distribute from the state of minimum momentum to that of the highest momentum called the Fermi momentum. Since there exists one quantum state for each volume $(2\pi\hbar)^3$ in the phase space, it holds

$$A = \frac{V}{(2\pi\hbar)^3} \int_0^{\hbar k_\mathrm{F}} p^2 \mathrm{d}p \mathrm{d}\Omega_p \times 2 \times 2 \tag{2.39}$$

if we represent the Fermi momentum as $p_\mathrm{F} = \hbar k_\mathrm{F}$. The last factor 2×2 is the statistical weight in the spin and isospin spaces. Hence we obtain

$$k_\mathrm{F} = \left(\frac{3\pi^2}{2}\right)^{1/3} \rho^{1/3} = \left(\frac{9\pi}{8}\right)^{1/3} \frac{1}{r_0} \tag{2.40}$$

by using Eq. (2.27). Similarly to the density, the Fermi momentum also does not depend on the mass number. The Fermi wave number is proportional to the $1/3$ power of the density as one can expect from the consideration of their dimensions.

Table 2.2 Nucleon number density, average nucleon distance, Fermi wave number, velocity, Fermi energy

r_0 (fm)	ρ(fm^{-3})	a (fm)	k_F (fm^{-1})	v_F/c	E_F (MeV)
1.10	0.179	1.77	1.38	0.29	39.5
1.15	0.157	1.85	1.32	0.28	36.1
1.20	0.138	1.94	1.27	0.27	33.1

Table 2.2 shows the number density of nucleons, average distance between nucleons a, Fermi wave number k_F, the speed of nucleon at the Fermi surface in units of the speed of light in vacuum v_F/c and the Fermi energy E_F for three representative values of r_0. The table shows that the speed of nucleons in the nucleus is at most 30% of the speed of light in vacuum. It is the reason why we adopt the non-relativistic theory to describe nuclei in most part of this book.[15]

Exercise 2.7 Show that the mass density of nuclei $\rho_{\rm mass}$ is about 2.9×10^{14} g/cm^3 by assuming that $\rho = 0.17\,{\rm fm}^{-3}$.

Sidebar 1: Why don't stars collapse? It looks puzzling that stars do not collapse despite the fact that the attractive gravitational forces are acting between the constituent particles. This is because the collapse is prevented by the *degeneracy pressure* of electrons and of other constituent particles in the star. As stated in the main text, all the fermions cannot occupy the smallest momentum state due to the Pauli exclusion principle. Instead, they distribute up to the Fermi surface with high momentum. The resulting pressure of the quantum mechanical origin, i.e., due to the Pauli exclusion principle, is the degeneracy pressure. The Fermi momentum increases and hence the degeneracy pressure increases if the volume of a star decreases by starting collapse. It is why stars do not collapse so easily. On the contrary, if the density of fermions such as electrons inside a star decreases for some reason, then the star starts to collapse because of the break-down of the balance between the attraction by the gravitational force and the degeneracy pressure. For example, a supernova explosion is initiated by the electron capture as we will describe in Sect. 2.3.

Exercise 2.8 Show that the degeneracy pressure of electrons is given by

$$P = \left(\frac{3}{\pi}\right)^{2/3} \frac{1}{20 m_{\rm e}} h^2 \rho^{5/3} \tag{2.41}$$

with the density of electrons ρ and the mass of electron $m_{\rm e}$ by using the fact that the pressure P is given by $P = -\partial E/\partial V$ when the temperature is zero, and by identifying the energy E with the total kinetic energy of electrons. Note that particles with

[15] One can take the opposite point of view that 30% is a large number. The relativistic descriptions of nuclear structure and nuclear reactions are also actively going on based on that point of view. The relativistic treatment has the advantage that the spin of nucleons is naturally introduced. In this book, we only touch the general framework of the relativistic mean-field theory in Sect. 6.3.

smaller mass work more effectively, i.e., give larger contribution, to the degeneracy pressure if the number densities of different particles are the same as Eq. (2.41) shows.

Sidebar 2: Why don't atoms collapse? A similar question arises for the size of atoms. Let us consider the neutral hydrogen atom as the example. The attractive Coulomb force acts between the proton and the electron in the hydrogen atom. The corresponding potential energy is given by $V(r) = V_C(r) = -e^2/r$ when they are separated by the distance r. It therefore looks energetically most stable at $r = 0$, i.e., when the proton and the electron stick to each other. Nonetheless, the size of the Hydrogen atom is known to be the Bohr radius given by $a_{\rm B} = 0.5 \times 10^{-8}\,{\rm cm}$, which is larger than the radius of proton $R_{\rm p} \sim 0.8 \times 10^{-13}\,{\rm cm}$ by 5 orders of magnitude. This is also a consequence of quantum mechanics. The world of quantum mechanics, i.e., the microscopic world, is governed by the uncertainty principle $\Delta x_\alpha \Delta p_\alpha \gtrsim \hbar$. On the other hand, the Hamiltonian describing the motion of the electron around the proton is given by $H = \frac{p^2}{2\mu} + V_C(r)$. Therefore, the uncertainty relation leads to approximately $E \gtrsim \frac{\hbar^2}{2\mu}(\frac{1}{r})^2 - \frac{e^2}{r}$ for the corresponding energy. The kinetic energy increases when r decreases and cancels the gain of the Coulomb energy, and even leads to a positive total energy. The radius of the Hydrogen atom, i.e., the Bohr radius $a_{\rm B}$, is obtained as the value of r which minimizes the energy E.

Sidebar 3: Atoms should have collapsed if the uncertainty principle or the commutation relation were absent Since the uncertainty principle is derived from the commutation relation $[\hat{x}_\alpha, \hat{p}_\beta] = {\rm i}\hbar\delta_{\alpha\beta}$, where $\hat{O}$ is the operator corresponding to an observable O, atoms would become point particles if the commutation relation did not govern the nature.

Sidebar 4: Application to Screening Effect As we learnt in Sect. 1.4 concerning the nuclear reactions in the Sun, many nuclear reactions in stars occur by quantum tunneling through the potential barrier called the Coulomb barrier made by the long-range Coulomb interaction. An interesting phenomenon in this connection is the screening effect caused by the surrounding charged particles which are in the plasma state in hot stars. It leads to an enhancement of the tunneling effect. Recently, the screening effect is argued also in connection with laboratory experiments, where low-energy nuclear reactions are caused in matter, e.g., in host metals [11]. It is reported that the reaction rate is enhanced and the screening effect is considered to be one of the origins of the enhancement. The interest is whether the enhancement of the reaction rate by the screening effect due to the presence of the host material is large and can explain the observed enhancement [12].

Let us denote the effective Coulomb potential, i.e., the screened Coulomb potential, around a nucleus with electric charge Ze by $\varphi(r)$. If we represent the change of the density of a charged particle ζ with the electric charge $Z_\zeta e$ in the surrounding induced by this nucleus as $\delta\rho_\zeta(\mathbf{r})$, then $\varphi(\mathbf{r})$ obeys the Poisson equation

$$\Delta\varphi(\mathbf{r}) = -4\pi \left[Ze\delta(\mathbf{r}) + \sum_{\zeta} Z_{\zeta} e \delta\rho_{\zeta}(\mathbf{r}) \right] . \tag{2.42}$$

The nuclear reactions in matter at laboratories are performed at the room temperature. Hence, we can use the Thomas–Fermi approximation for the density of electrons of the host material, and obtain

$$\varphi(\mathbf{r}) = \frac{Ze}{r} \exp(-q_{\mathrm{TF}} r) \tag{2.43}$$

for the solution of Eq. (2.42) within the framework of the linear approximation, where the inverse of the screening length q_{TF} is given by

$$q_{\mathrm{TF}} = \sqrt{\frac{6\pi\rho_0}{\varepsilon_{\mathrm{F}}^{(0)}} e^2} . \tag{2.44}$$

The ρ_0 and $\varepsilon_{\mathrm{F}}^{(0)}$ are the density of free electrons in the metal and the Fermi energy, respectively, before they are polarized.

On the other hand, for nuclear reactions in hot stars, the densities of the charged particles composing the plasma are well represented by the Boltzmann distribution. Consequently, the screened potential is given by the following well-known *Debye–Hückel formula*,

$$\varphi(\mathbf{r}) = \frac{Ze}{r} \exp(-\kappa_{\mathrm{DH}} r) , \tag{2.45}$$

$$\kappa_{\mathrm{DH}} = \sqrt{4\pi\beta e^2 \sum_{\zeta} Z_{\zeta}^2 \rho_{\zeta}^{(0)}} , \tag{2.46}$$

where $\beta = 1/kT$, where k and T are the Boltzmann constant and the temperature of the star, respectively.

Exercise 2.9 Derive Eqs. (2.44) and (2.46).

2.3 Nuclear Masses

We denote the mass of the nucleus with the mass number A and the atomic number Z by $M(A, Z)$. The nuclear mass is one of the basic quantities of each nucleus. At the same time, it is a fundamental quantity which governs various nuclear reactions.

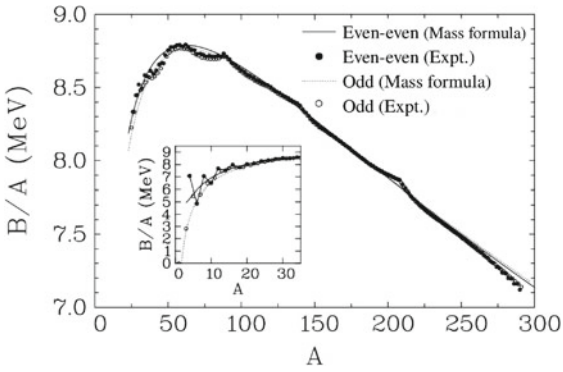


Fig. 2.6 The binding energy per nucleon as a function of the mass number A [13]

2.3.1 *The Binding Energies: Experimental Data and Characteristics*

One usually uses the *binding energy* $B(A, Z)$ for the mass $M(A, Z)$ in various discussions. The $B(A, Z)$ is defined as the energy gain obtained by forming a nucleus instead of being completely apart as individual nucleons. It is therefore given by[16,17]

$$B(A, Z) = ZM_{\mathrm{p}}c^2 + (A - Z)M_{\mathrm{n}}c^2 - M(A, Z)c^2 . \tag{2.48}$$

The filled circles in Fig. 2.6 show the experimental value of the binding energy per nucleon B/A for the most stable even–even nucleus for each mass number, and the open circles that for the most stable nucleus in the case of odd mass number.[18] The inset shows the details for nuclei with small mass number, i.e., for light nuclei. The binding energy has the following characteristics including those shown in these figures.

(1) The binding energy rapidly increases with the mass number in the region of small mass number (see Table 2.3).[19]

---

[16]The *separation energy* is also an important related physical quantity. It is the energy needed to remove a particle such as a nucleon or an alpha particle from the nucleus. For example, the separation energy of neutron is given by $S_n(N, Z) \equiv B(A, Z) - B(A - 1, Z)$ in terms of the binding energies of the relevant nuclei.

[17]The binding energy of a nucleus is usually calculated from the mass of the corresponding neutral atom $M_{\mathrm{atom}}(A, Z)$ as

$$B(A, Z) = ZM_{\mathrm{H}}c^2 + (A - Z)M_{\mathrm{n}}c^2 - M_{\mathrm{atom}}(A, Z)c^2 , \tag{2.47}$$

where M_{H} is the mass of the Hydrogen atom.

[18]Exactly speaking, they have been obtained by using Eq. (2.47).

[19]We name deuteron and triton and denote by d and t in the case of nuclei, while name deuterium and tritium and denote by D and T in the case of neutral atoms.

Table 2.3 Binding energies of some light nuclei

Nuclide	d ($^{2}_{1}$H)	t ($^{3}_{1}$H)	$^{3}_{2}$He	α ($^{4}_{2}$He)
Binding energy (MeV)	2.225	8.482	7.718	28.296

Table 2.4 Correlation between the even–odd property of the proton and neutron numbers and the stability of nuclei. The δ represents a systematic variation which appears in the binding energy B in connection with the even–odd property of the proton and neutron numbers. The Δ is called the *odd–even mass parameter*

A	Z	N	Stability	Pairing correlation energy δ (MeV)
Even	Even	Even	Most stable	$\Delta \approx 12/\sqrt{A}$
Odd	Even	Odd	Less stable	0
Odd	Odd	Even	Less stable	0
Even	Odd	Odd	Least stable	$\Delta \approx -12/\sqrt{A}$

(2) The B/A shows a sharp maximum at each light α-nucleus.[20,21]
(3) The binding energy per nucleon B/A is always about 8 MeV except for light nuclei (*saturation property of the binding energy*).
(4) Roughly speaking, the B/A steadily increases with the mass number until the region of Fe whose atomic number is 26,[22] then gradually decreases with A.
(5) The B/A shows local maxima when the number of either protons or neutrons takes special numbers, e.g., $Z = 50$, in the region of large mass number.
(6) There exist systematic dependences on the even–odd property of the number of protons and that of neutrons as shown in Table 2.4.[23,24]

Let us introduce here a few topics associated with the characteristics of the binding energy mentioned from (1) through (6).

Topic 1: The Energy Generation in the Main Sequence Stars The characteristic (1) mentioned above is the reason why the energy is generated by nuclear fusion in stars in the main sequence. The binding energies of light nuclei including the values

[20] Those nuclei such as $^{8}_{4}$Be, $^{12}_{6}$C, $^{16}_{8}$O whose atomic number and the mass number are the same multiples of those of α particle are called α-nuclei.

[21] The binding energy of $^{8}_{4}$Be is less than twice that of α by 0.1 MeV, so that $^{8}_{4}$Be is unstable and exists only transiently.

[22] The nucleus which has the largest value of B/A is $^{62}_{28}$Ni (see [14]).

[23] Only 5 nuclei, i.e., d, $^{6}_{3}$Li, $^{10}_{5}$B, $^{14}_{7}$N, $^{180}_{73}$Ta (isomer), are stable among the so-called odd–odd nuclei, which have odd numbers for both the proton and the neutron numbers. Incidentally, it is $^{209}_{83}$Bi which has the largest atomic number among stable nuclei, although exactly speaking it decays with the half-life of 1.9×10^{19} years. There exist no stable isotopes for Tc and Pm, whose atomic numbers are 43 and 61, respectively.

[24] It is related to the pairing correlation between nucleons, which will be discussed later in detail.

listed in Table 2.3 are the important quantities to determine the energies released by those nuclear reactions and also the energies of the emitted particles such as neutrinos.

The nuclear reactions which power the main sequence stars can be classified into (a) *pp-chain (proton–proton chain)* reactions, which consist of ppI-chain, ppII-chain and ppIII-chain reactions, and (b) *CNO cycle*. Their reactions and the associated energy releases are as follows:

- ppI chain

① $\mathrm{p}+\mathrm{p} \rightarrow {}^{2}\mathrm{H}+\mathrm{e}^{+}+\nu_{\mathrm{e}}+0.42\,\mathrm{MeV} \quad (\nu_{\mathrm{pp}})$
② $\mathrm{e}^{+}+\mathrm{e}^{-} \rightarrow 2\gamma+1.02\,\mathrm{MeV}$
③ ${}^{2}\mathrm{H}+\mathrm{p} \rightarrow {}^{3}\mathrm{He}+\gamma+5.49\,\mathrm{MeV}$
④ ${}^{3}\mathrm{He}+{}^{3}\mathrm{He} \rightarrow {}^{4}\mathrm{He}+2\mathrm{p}+12.86\,\mathrm{MeV}$

- ppII chain

⑤ ${}^{3}\mathrm{He}+{}^{4}\mathrm{He} \rightarrow {}^{7}\mathrm{Be}+\gamma$
⑥ ${}^{7}\mathrm{Be}+\mathrm{e}^{-} \rightarrow {}^{7}\mathrm{Li}+\nu_{\mathrm{e}} \quad (\nu_{\mathrm{Be}})$
⑦ ${}^{7}\mathrm{Li}+\mathrm{p} \rightarrow 2\,{}^{4}\mathrm{He}$

- ppIII chain

⑧ ${}^{7}\mathrm{Be}+\mathrm{p} \rightarrow {}^{8}\mathrm{B}+\gamma$
⑨ ${}^{8}\mathrm{B} \rightarrow {}^{8}\mathrm{Be}+\mathrm{e}^{+}+\nu_{\mathrm{e}} \quad (\nu_{\mathrm{B}})$
⑩ ${}^{8}\mathrm{Be} \rightarrow 2\,{}^{4}\mathrm{He}$

- CNO cycle

⑪ ${}^{12}\mathrm{C}+\mathrm{p} \rightarrow {}^{13}\mathrm{N}+\gamma+1.94\,\mathrm{MeV}$
⑫ ${}^{13}\mathrm{N} \rightarrow {}^{13}\mathrm{C}+\mathrm{e}^{+}+\nu_{\mathrm{e}}+1.20\,\mathrm{MeV}$
⑬ ${}^{13}\mathrm{C}+\mathrm{p} \rightarrow {}^{14}\mathrm{N}+\gamma+7.55\,\mathrm{MeV}$
⑭ ${}^{14}\mathrm{N}+\mathrm{p} \rightarrow {}^{15}\mathrm{O}+\gamma+7.29\,\mathrm{MeV}$
⑮ ${}^{15}\mathrm{O} \rightarrow {}^{15}\mathrm{N}+\mathrm{e}^{+}+\nu_{\mathrm{e}}+1.74\,\mathrm{MeV}$
⑯ ${}^{15}\mathrm{N}+\mathrm{p} \rightarrow {}^{12}\mathrm{C}+{}^{4}\mathrm{He}+4.97\,\mathrm{MeV}$
⑰ $\mathrm{e}^{+}+\mathrm{e}^{-} \rightarrow 2\gamma+1.02\,\mathrm{MeV}$

We introduced the notations ν_{pp}, ν_{Be}, ν_{B} to distinguish neutrinos of different origins.

By adding the nuclear reactions in ①–④ with appropriate weights, one can see that the energy of 26.72 MeV in total is released by converting four protons into one ${}^{4}\mathrm{He}$ nucleus in the ppI chain,

$$4\mathrm{p}+2\mathrm{e}^{-} \rightarrow {}^{4}\mathrm{He}+2\nu_{e}+26.72\,\mathrm{MeV}. \tag{2.49}$$

Also for the CNO cycle, we obtain the same net reaction formula as Eq. (2.49) by adding ⑪–⑯ and subtracting twice of ⑰ on each side. The central temperature of the Sun is about 16 million K, and the standard solar model predicts that about 98.5% of the solar energy is produced by nuclear reactions in the pp chain, while the remaining about 1.5% by the CNO cycle.

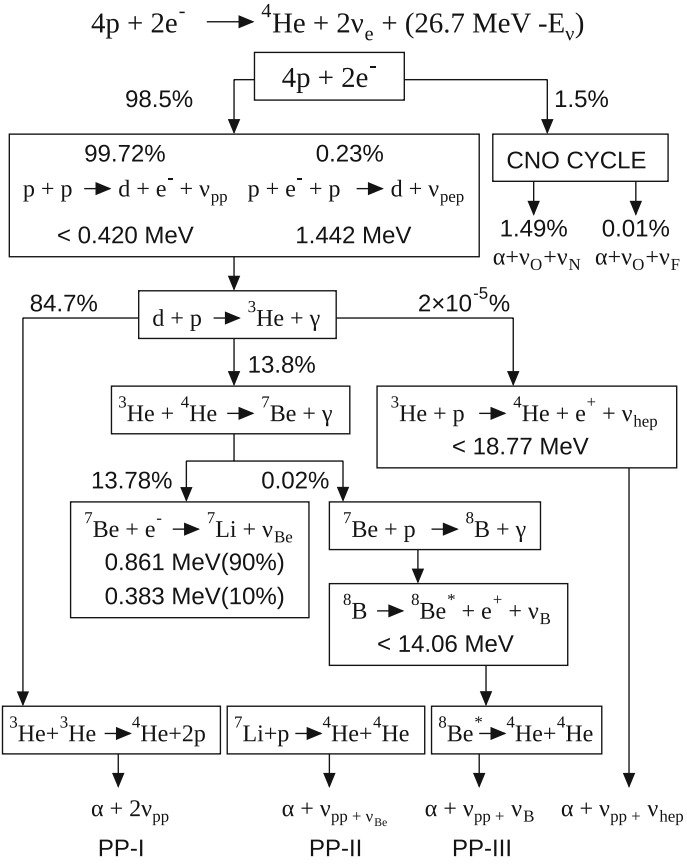


Fig. 2.7 Conceptual representation of the pp chain and CNO cycle. Taken from [15]

Figure 2.7 represents conceptually the pp chain and the CNO cycle, and Fig. 2.8 the spectra of solar neutrinos emitted by various reactions. Note that two-body reactions lead to line spectra, while three-body reactions continuous spectra. Experimentally, the high-energy neutrino ν_B is detected either by water Cherenkov detectors or by using the reaction of ^{37}Cl,

$$\nu_e + {}^{37}\mathrm{Cl} \rightarrow {}^{37}\mathrm{Ar} + \mathrm{e}^- \,. \tag{2.50}$$

The low-energy neutrino ν_{pp} is studied, on the other hand, through the capture reactions by Ga and deuterium.

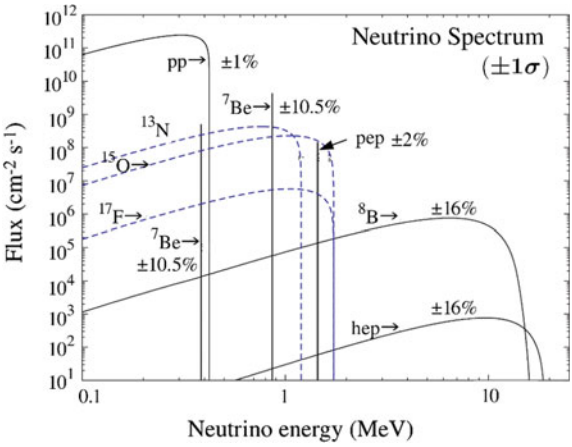


Fig. 2.8 The solar neutrino spectra. Taken from [16]. The *solid lines* are the spectra for the pp chain and the *dashed lines* those for the CNO cycle

The *solar neutrino problem*[25] was a serious problem, which lasted from mid-1960s to the beginning of the twenty-first century. It is now attributed to the neutrino oscillation.

Topic 2: The Energy Problem: *Muon-Catalysed Fusion (μCF)* The binding energies of light nuclei listed in Table 2.3 are important quantities in connection with the so-called energy problem as well. For example, if the nuclear reactions $p+d \rightarrow {}^3He$, $d+t \rightarrow {}^4He+n$ take place, the energy of 5.4 and 17.5 MeV is released per reaction for the two cases, respectively. However, like the $p+p \rightarrow d+e^+ + \nu_e$ reaction in the Sun mentioned in Sect. 1.4, the high Coulomb barrier between the projectile and target nuclei has to be overcome in order for these reactions to occur. The so-called high-temperature fusion reactions attempt to overcome the Coulomb barrier by heating the nuclei to high temperature. In this case, the nuclei of high temperature need to be confined in a small space. To that end, various methods such as the magnetic confinement, where the hot fusion fuel is confined by magnetic fields in a small space in the form of plasma, and the inertial confinement have been developed. However, none of the methods have yet reached the practical usage for the power production. The muon-catalysed fusion is an alternative method, where one tries to induce fusion reactions at low temperature by lowering the Coulomb barrier with the screening effect by μ^- particle.

Figure 2.9 shows the muon-catalysed pd fusion which has been confirmed experimentally for the first time as the evidence of the μCF.[26] Figure 2.10 conceptually shows the muon-catalysed dt fusion which is currently thought to be most promis-

[25] It is the problem that the observed number of solar neutrinos is only about 1/2–1/3 of the theoretical prediction.

[26] In 1956, Alvarez et al. discovered a trajectory of muon which stops in the liquid hydrogen contaminated with deuterium. The flight length in matter is determined by the stopping power. The length 1.7 cm of the trajectory observed by Alvarez et al. exactly matched the flight length of muon with energy of 5.4 MeV which is released in the $p+d \rightarrow {}^3He$ reaction.

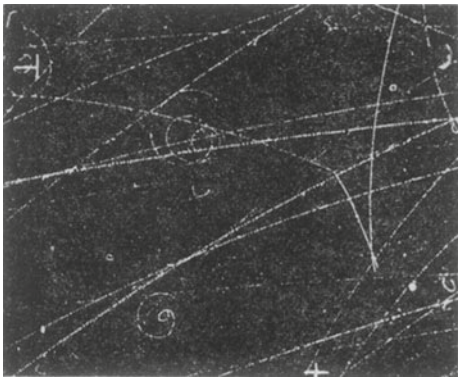


Fig. 2.9 The first experimental evidence of the μCF. Taken from [17]

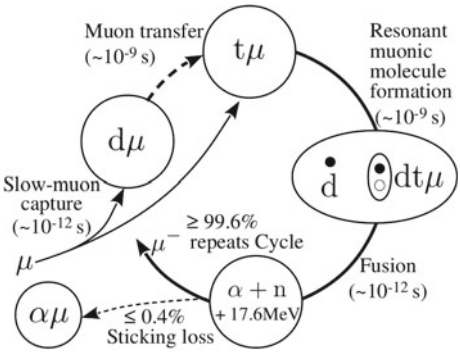


Fig. 2.10 The μCF cycle. $dt\mu \rightarrow {}^4He + n + \mu + 17.5$ MeV reaction. Taken from [18]

ing from the point of view of the practical usage for the power production. In the latter, the liquid target of the mixture of about 50% each of deuterium and tritium is injected by μ^- particle produced by nuclear reactions. Thus produced $d\mu$ and $t\mu$ atoms collide to form a $dt\mu$ molecule. Eventually the nuclear reaction

$$d + t \rightarrow \alpha + n \tag{2.51}$$

takes place. The μ^- particle which stimulated tunneling effect through screening the Coulomb barrier finishes the role of a catalyst by forming a muonic atom by sticking to the α particle produced in the nuclear reaction with a certain probability. However, with a much higher probability it leaves the nucleus by using a part of the energy released in the reaction, and repeats the cycle as a catalyst. Whether the muon-catalysed fusion is useful for the practical usage for the energy generation or not depends on the number of cycle per muon, whose mean life is 2.2 μs, and the reactivation probability by collision of the muon lost by forming a muonic atom such as $\alpha\mu$. The $dt\mu$ reaction is more promising than the $pd\mu$ reaction, because the $dt\mu$ molecule is produced resonantly by the so-called *Vesman mechanism*, and also because the sticking probability is smaller (see [18] for details).

Finally, we wish to refer to the nuclear reaction in matter [11] as a closely related research. It is the study, for example, to see whether the rates of the $d+d \to t+p$, ^3He+n reactions are significantly enhanced over those in the free space if a metal target such as Pd and PdO is continuously bombarded with deuterons.

Topic 3: The Alpha Particle Model and Cluster Structures *Symmetry* plays important roles in physics. The characteristic (2) of the binding energy mentioned in Sect. 2.3.1 originates from the property of nuclear force that favours states with good spatial symmetry. Historically, based on this property, the model called *the α-particle model* has been proposed which views the light α-nuclei as aggregates of α particles and describes their ground states and low-lying excited states by special spatial configurations or relative motions of the constituent α particles or by the rotations of the whole nucleus. In this model, for example, the ground state of ^{12}C is thought to be an equilateral triangle configuration of three α particles, while the ground state of ^{16}O a regular tetrahedron of four α particles. In these days, the standard model for nuclear structure is the *shell model* which views the nucleus as an ensemble of nucleons which are moving independently from each other in a common mean field of a single center in the zeroth order approximation (see Chap. 5). On the contrary, the α-particle model is a *molecular point of view* or a *molecular structure model* which assumes the existence of multi-centers or of density localization. This idea has been extended to variational calculations and currently to the *cluster model* (the study of cluster structure) by using the mean-field theory or the *molecular dynamics calculations*, and intensive studies are going on from that points of view. The molecular structures are expected to appear at the energies near the threshold energy for each molecular structure, and are characterized by having a large decay width to each corresponding decay channel as an indicator. Figure 2.11 shows[27] the excitation energy of various molecular structures in light nuclei expected from this idea. It is called the Ikeda diagram (see [20, 21] for details of the study of cluster structure).

Figure 2.12 shows the energy-level diagram of ^{12}C in the region of low excitation energies [22] in order to help a deeper understanding. The second 0^+ state denoted by 0_2^+ at the excitation energy 7.65 MeV, which is close to the threshold energy for the α-decay 7.37 MeV, is a state for which the 3α-particle model works well.[28] The ground state locates somewhat far from the threshold energy for the α-decay. Consequently, the density localization becomes less significant. Nevertheless, the picture that the state consists of 3α-clusters which form an equilateral triangle configuration is still valid to some extent. One can think that it is an experimental evidence that there appears a 3^- state at a low excitation energy, i.e., at 9.64 MeV, which is expected from the D_{3h} symmetry of the point group associated with the equilateral triangle configuration. The existence of a rotational band, $0_{g.s.}$, 2_1^+ (4.44 MeV), 4_1^+ (14.08 MeV $\approx$ 4.44 MeV $\times$ 3.33) also supports this point of view. However, if there

[27] The threshold energies for α-decay, and those for emitting several α particles, and also the threshold energy of the decay of ^{24}Mg into two ^{12}C nuclei, taken from [19].

[28] The synthesis of ^{12}C in stars proceeds as $^8Be+\alpha \to {}^{12}C(0_2^+)$, $^{12}C(0_2^+) \to {}^{12}C(0_{g.s.}^+)$ In that sense, the 0_2^+ state of ^{12}C plays a crucial role in the synthesis of heavy elements, and is named *Hoyle-state* after F. Hoyle who predicted the existence of this state.

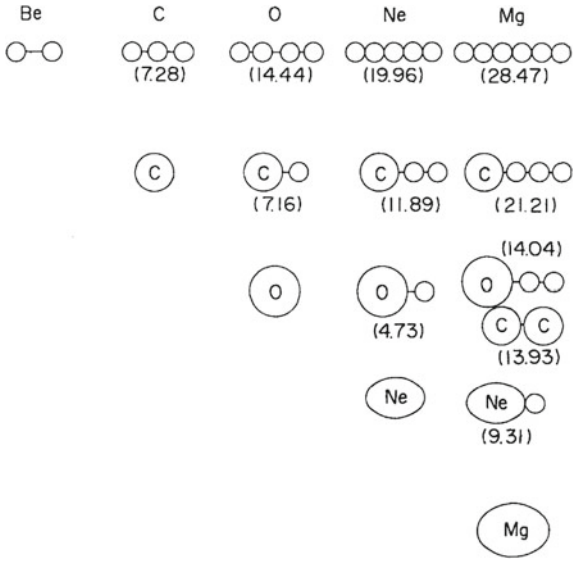


Fig. 2.11 The Ikeda diagram: Threshold energies corresponding to various cluster structures [19]

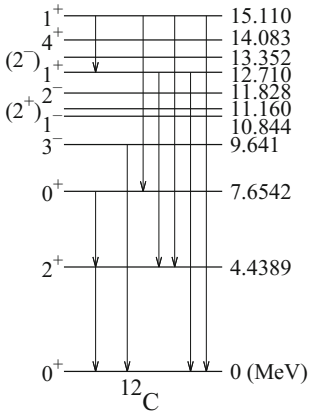


Fig. 2.12 The low-lying energy levels of ^{12}C

appear states only up to 4^+ member, the rotational property of the spectrum can be explained also by a usual shell model without assuming the density localization (*Elliott's SU*(3) *model*). A more accurate description of the ground state and the ground-state rotational band is provided by a *hybrid model*, which hybridizes the α-cluster model and the shell model in order to take into account the broken spatial symmetry due to the spin–orbit interaction [23].[29] Incidentally, the cluster structure

[29] In the case of ^{12}C, the spin–orbit interaction reduces the extent of deformation and increases the excitation energy of the 2_1^+ state. From the point of view of shell model, a force with smaller spin–orbit splitting leads to a high degeneracy and to a larger deformation due to the Jahn–Teller effect, while a force with a strong spin–orbit force leads to a large splitting between the $p_{3/2}$ and

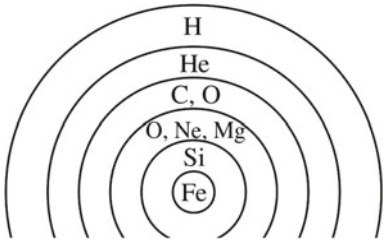


Fig. 2.13 The onion layer structure of a presupernova star

and the deformation of nuclei, which is described in detail in Chap. 7 can be thought to be a kind of *Jahn–Teller effect*.[30]

Exercise 2.10 Let us assume that three α particles form an equilateral triangle, i.e., the D_{3h} state of the point group. Show that in this case the component of the angular momentum along the axis perpendicular to the plane made by the three α particles, which is called the K quantum number, takes only multiples of 3.

Topic 4: The Onion Layer Structure of a Massive Star and the Iron Core In massive stars whose mass M exceeds 12 times the solar mass, i.e., $M > 12M_{\odot}$, there exists a core consisting of Fe and Ni at the center and successive layers of gradually smaller atomic number distribute towards the surface (*onion layer structure*). Figure 2.13 shows the inner structure of a presupernova star. The core part consists of Fe and Ni, because the binding energy per particle becomes the largest in the Fe region as remarked in Sect. 2.3.1 as the characteristic (4) of the binding energy per nucleon B/A.[31,32] For the same reason, nuclei with small atomic number and mass

(Footnote 29 continued)
$p_{1/2}$ states. Consequently, the degeneracy disappears and the spherical shape is predicted to appear. Inversely, if one considers from the point of view of the cluster model, too large deformation or clusterization is predicted and consequently the excitation energy of the 2_1^+ state becomes too low compared with the experimental data if one assumes the cluster state which extends the pure state of the maximum spatial symmetry of the shell model denoted by $(0s)^4(0p)^8[444]^{11}L$ configuration by introducing a finite distance between three alpha clusters, but ignores the spin–orbit interaction, and the experimental data can be well reproduced by admixing states with lower spatial symmetry by the spin–orbit interaction.

[30] In the case when the electronic states degenerate in energy in a polyatomic molecule where the atoms have a highly symmetric geometrical configuration such as a regular polyhedron, it becomes energetically more stable if the degeneracy is removed by assuming a configuration of atoms with lower symmetry. This is known as the Jahn–Teller effect. Similar situations occur in many physical systems including metal microclusters.

[31] A statement often appears in the literature that the central part of massive stars consists of $^{56}_{26}$Fe due to the fact that the nucleus which has the largest binding energy per nucleon is $^{56}_{26}$Fe. However, in reality, the nucleus which has the maximum binding energy per nucleon is $^{62}_{28}$Ni. It is understood that the reason why the major component of the core is $^{56}_{26}$Fe despite this fact is because $^{62}_{28}$Ni is hard to be synthesized by nuclear reactions in stars, while $^{56}_{26}$Fe can be easily synthesized as the last nucleus in the Si-burning reaction.

[32] The temperature of the central part has to be sufficiently high in order for the core of Fe and Ni to be formed in the central part of stars. In the stars whose mass is not so large, the central part

number proceed towards Fe and Ni by fusion reactions. On the contrary, nuclei with large atomic number and mass number proceed to Fe and Ni by fission.

Topic 5: The Supernova Explosion It is known that there exist two types of supernova explosion, i.e., that initiated by carbon detonation and by gravitational collapse.[33] In the latter case, and in massive stars whose core part is made of Fe and Ni, the gravitational collapse is triggered when Fe in the core captures surrounding electrons by *electron capture reaction*,

$$^{56}_{26}\mathrm{Fe} + \mathrm{e}^- \rightarrow {}^{56}_{25}\mathrm{Mn} + \nu_\mathrm{e}\,, \tag{2.52}$$

and consequently when the degeneracy pressure of electrons decreases. Also, if the central temperature exceeds 5×10^9 K, an endothermic photo-disintegration reaction of Fe,

$$^{56}_{26}\mathrm{Fe} + \gamma \rightarrow 13\,{}^4\mathrm{He} + 4\mathrm{n} - 125\,\mathrm{MeV}, \tag{2.53}$$

takes place in addition, and at higher temperatures, the photo-disintegration reaction of ^{4}He,

$$^4\mathrm{He} + \gamma \rightarrow 2\mathrm{n} + 2\mathrm{p} - 28.3\,\mathrm{MeV}, \tag{2.54}$$

occurs as well. The internal energy which should have increased by contraction does not lead to the increase of the pressure by being used in these endothermic reactions. Thus, the contraction of the star cannot be prevented. Consequently, the gravitational collapse of the star proceeds and eventually is bounced back by the hard core in the nuclear force (see Sect. 3.7) when the density increases so high as nucleons start to overlap. The collapse thus changes into explosion and neutrinos and many other particles are emitted into space. This is a scenario of the supernova explosion. The supernova explosion is an interesting subject to be studied also in connection with the synthesis of elements, e.g., as a site to synthesize heavy elements such as U by *rapid neutron capture reactions* called *r-process*.

Exercise 2.11 Show that the thermal pressure in high temperature ideal gas is given by

$$P_T = \rho T \tag{2.55}$$

in terms of the temperature T and the density ρ. (Hint: Assume that the momentum distribution of the gas is given by the Boltzmann distribution. See Sect. 6.2.5.)

(Footnote 32 continued)
therefore consists of nuclei with smaller mass number than that of Fe, though they have an onion layer structure. For example, the central part of stars whose mass lies between $8M_\odot < M < 12M_\odot$ consists of O, Ne and Mg.

[33] There is an alternative way to classify the supernova explosion into the type II and I, respectively, depending on whether the spectrum contains the hydrogen line or not.

2.3.2 The Semi-empirical Mass Formula (The Weizsäcker–Bethe Mass Formula)—The Liquid-Drop Model

The bulk behaviour of the binding energy can be well represented by a simple formula

$$B = b_{\text{vol}} A - b_{\text{surf}} A^{2/3} - \frac{1}{2} b_{\text{sym}} \frac{(N-Z)^2}{A} - b_{\text{C}} \frac{Z^2}{A^{1/3}} + \delta(A)\,, \tag{2.56}$$

which takes into account major physical effects. Equation (2.56) is called the *Weizsäcker–Bethe mass formula*.[34] The first and the second terms on the right-hand side are called the volume and the surface[35] terms, respectively, because the nuclear radius is proportional to $A^{1/3}$. The property that the bulk binding energy is the volume term which is proportional to the number of constituent particles comes from the fact that the nuclear force which stabilizes a nucleus as an isolated bound system is of short range as we learn in the next chapter. The existence of the surface term will be easily understood from the point of view of the liquid-drop model for nuclei. The third term is called the *symmetry energy term* and tends to locate stable nuclei along the diagonal line in the nuclear chart. We will learn its origin later somewhat in detail. The fourth term represents the effect of *Coulomb energy*. As we have already remarked in Sect. 2.3.1 the last term originates from the pairing correlation between nucleons and represents the fact that the binding energy systematically changes according to the even–odd property of the atomic number and of the neutron number. It will be described in detail in Sect. 5.8.

The values of the parameters in the mass formula somewhat vary depending on the experimental data to be reproduced. The solid line in Fig. 2.6 represents the theoretical values given by the mass formula when the parameters $b_{\text{vol}}, b_{\text{surf}}, b_{\text{sym}}, b_{\text{C}}$ are determined by the least-square fit to the binding energies of even–even nuclei for which $N, Z > 7$ and the experimental error of the binding energy B is smaller than 200 keV [25]. We fixed the δ for the pairing correlation to be $\delta = 12/\sqrt{A}\,\text{MeV}$. The dotted line represents the similar fit to odd nuclei. In both cases, the fitting was performed to the most stable isobar for each mass number A, i.e., the experimental data shown in the figure. We observe that the mass formula well reproduces the bulk behaviour of the binding energy. Thus obtained values of the parameters are listed in Table 2.5.

Comment: The Reason Why Stable Nuclei Locate along the Diagonal Line of the Nuclear Chart: The Symmetry Energy and Its Origin As stated above, the symmetry energy locates stable nuclei nearly along the diagonal line in the nuclear chart. Let us consider the contribution of the kinetic energy to the binding energy in

[34] At present, there exist several refined mass formulae [24] reflecting various studies such as those of unstable nuclei, superheavy elements and nucleosynthesis of elements through r-process. In those refined mass formulae, for example, the effects of surface diffuseness and of the symmetry energy correction to the volume as well as the surface terms are considered.

[35] If we define the *nuclear surface tension* σ by $\sigma \equiv b_{\text{surf}} A^{2/3}/4\pi(r_0 A^{1/3})^2$, then $\sigma \sim 1\,\text{MeV/fm}^2$.

Table 2.5 The values of parameters in the mass formula used to obtain the solid and dotted lines in Fig. 2.6. All the values are in units of MeV

	b_{vol}	b_{surf}	b_{sym}	b_{C}	δ
Even–even (solid line)	16.2	19.0	47.0	0.755	$12/\sqrt{A}$
Odd (dotted line)	16.3	19.2	45.4	0.770	0

order to understand the origin of the symmetry energy. If we use the Thomas–Fermi approximation, we have

$$E_{\mathrm{kin}} = E_{\mathrm{kin}}^{(\mathrm{n})} + E_{\mathrm{kin}}^{(\mathrm{p})} = \frac{3}{5}\varepsilon_{\mathrm{F}}^{(\mathrm{n})} N + \frac{3}{5}\varepsilon_{\mathrm{F}}^{(\mathrm{p})} Z \approx \frac{3}{5}\varepsilon_{\mathrm{F}} A + \frac{1}{3}\varepsilon_{\mathrm{F}} \frac{(N-Z)^2}{A}\,. \tag{2.57}$$

By comparing the second term on the right-hand side of Eq. (2.57) with the symmetry energy term in the mass formula, we obtain

$$b_{\mathrm{sym}}^{(\mathrm{kin})} = \frac{2}{3}\varepsilon_{\mathrm{F}} \sim 25\,\mathrm{MeV}. \tag{2.58}$$

The comparison of this value with the value of the parameter of the symmetry energy b_{sym} given in Table 2.5 shows that about half of the symmetry energy arises from the kinetic energy due to the Pauli exclusion principle (Pauli effect). The other half originates from the fact that the nuclear force in the isospin singlet term, i.e., that between n and p in the isospin singlet configuration, is stronger than that in the isospin triplet terms, i.e., that in the isospin triplet configurations of the pp, np and nn systems as we learn in the next chapter.

2.3.3 Applications of the Mass Formula (1): The Stability Line, the Heisenberg Valley

The mass formula is useful, for example, to predict the masses of unknown nuclei and also to discuss the bulk aspects concerning the stability of nuclei such as the stability with respect to fission. Here and in the next subsection, let us study some of the applications of the mass formula.

2.3.3.1 The Formula for the Stability Line

In the region of small atomic number, the stable nuclei locate along the diagonal line or in the vicinity in the nuclear chart. This is due to the symmetry energy term

in the mass formula. However, the contribution of the Coulomb energy becomes non-negligible as the atomic number gets large. Consequently, the location of stable nuclei gradually deviates from the diagonal line and the neutron number of stable nuclei becomes about 1.6 times the proton number ($N \sim 1.6Z$) in the region of large atomic number such as U. This trend can be derived from the mass formula. If we denote the atomic number of the most stable nucleus for a given mass number A_0 by $Z_{\beta s}(A_0)$, then $\frac{\partial}{\partial Z} B(A, Z)|_{A=A_0} = 0$ at $Z = Z_{\beta s}(A_0)$. Hence we obtain

$$Z_{\beta s}(A) = \frac{A/2}{1 + \frac{b_C}{2b_{\rm sym}} A^{2/3}} \approx \frac{A/2}{1 + 0.00803 A^{2/3}} \tag{2.59}$$

from the mass formula. We used the values listed in Table 2.5 in obtaining the third term. If we denote the value of Z in the case when we let $N = 1.6Z$ by $\tilde{Z}$, for example, $Z_{\beta s} = 61$, $\tilde{Z} = 58$ for $A = 150$, and $Z_{\beta s} = 81$, $\tilde{Z} = 80$ for $A = 208$, indicating that the values of $Z_{\beta s}$ and $\tilde{Z}$ are very close to each other. In fact, ${}^{150}_{62}$Sm and ${}^{208}_{82}$Pb are stable nuclei.[36] In this way, the ratio between the proton number and the neutron number for heavy nuclei is determined by the balance between the Coulomb energy and the symmetry energy.

2.3.3.2 The Heisenberg Valley

Figure 2.14 is a schematic three-dimensional representation of the nuclear mass M as a function of the neutron number N and the proton number Z. There exist three planes corresponding to the even–even, even–odd or odd–even, and odd–odd nuclei due to the pairing term δ in the mass formula. The line along a cross section represents the variation of the masses for a given isobars. It behaves like a quadratic function because of the symmetry energy. This property is shown in Fig. 2.15 for the nuclei with odd-mass number, and in Fig. 2.16 for even-A nuclei. As these figures

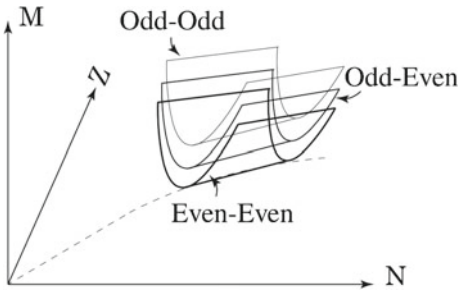


Fig. 2.14 The Z, N dependence of the nuclear mass: The Heisenberg valley

[36] ${}^{150}_{58}$Ce and ${}^{208}_{80}$Hg are unstable nuclei. The relationship $N \sim 1.6Z$ should be taken only as a rough relationship that holds in the region of large mass number. To be accurate, it is safer to use Eq. (2.59).

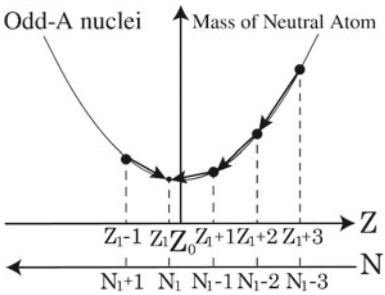


Fig. 2.15 The Z, N dependence of the nuclear masses of the isobars with an odd A

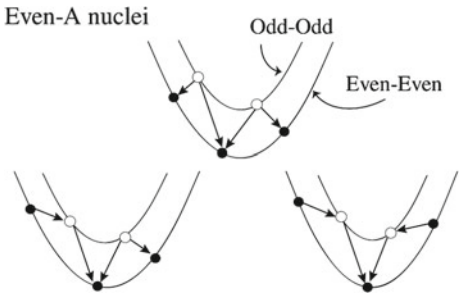


Fig. 2.16 The Z, N dependence of the nuclear masses of the isobars with an even A

show, there exist one stable nucleus in the case of odd A and 1–3 stable nuclei in the case of even A which are stable with respect to β-decay or electron capture.

These stable nuclei form a kind of valley in Fig. 2.14 as the mass number is varied. This valley is called the *Heisenberg valley*. Its projection on the NZ-plane follows almost along Eq. (2.59). The synthesis of light elements up to Fe by nuclear fusion and the synthesis of heavy elements up to Bi by the slow neutron capture reaction, called *s-process*, proceed along the Heisenberg valley.

Incidentally, the conditions for the β^--decay, β^+-decay and electron capture to occur are given by the following equations using the mass $M(A, Z)$ of the neutral atom of atomic number Z and mass number A, the mass of electron m_e and the binding energy Δ_e of the electron to be captured in the electron capture in the atom before it is captured,

$$M(A, Z) > M(A, Z+1) \quad \text{for } \beta^- \text{decay}, \tag{2.60}$$

$$M(A, Z) > M(A, Z-1) + 2m_e \quad \text{for } \beta^+ \text{decay}, \tag{2.61}$$

$$M(A, Z) > M(A, Z-1) + \Delta_e/c^2 \quad \text{for electron capture.} \tag{2.62}$$

Here, we ignored the change of the binding energy of electron associated with the change of atom.

Exercise 2.12 Prove Eqs. (2.60)–(2.62).

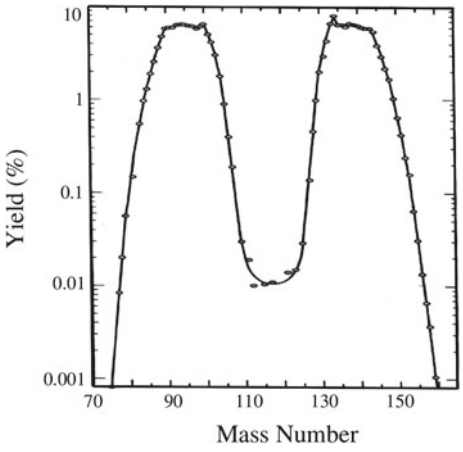


Fig. 2.17 The mass distribution of the fission fragments in the thermal-neutron-induced fission of $^{235}_{92}$U. Taken from [26]

2.3.4 Applications of the Mass Formula (2): Stability with Respect to Fission

Fission or nuclear fission is a process where a nucleus with a large atomic number such as U, Th and Pu disintegrates into two fragments, called fission fragments, with nearly equal mass numbers. As an example, Fig. 2.17 shows the mass distribution of the fission fragments in the thermal-neutron-induced fission of ^{235}U.[37] The fission was discovered by Hahn and Strassmann in 1938 [28].[38] Bohr and Wheeler gave a theoretical interpretation soon after the discovery of fission. The following discussions follow their paper [29].[39]

Figure 2.18 schematically represents a process, where a nucleus viewed as a liquid-drop disintegrates into two fission fragments of equal mass, i.e., of a *symmetric fission*.[40] The configuration d in the figure is called *scission point*.

---

[37] In the spontaneous fission or in the induced fission by a small energy, hence with low excitation energy, fission with a striking mass-asymmetry occurs as shown in Fig. 2.17 because of the shell effect which we study in Chap. 5. Also, a few neutrons are emitted simultaneously in each spontaneous fission and in each thermal neutron-induced fission. For example, the average numbers of neutrons emitted in thermal neutron-induced fission of ^{235}U and $^{239}_{94}$Pu are 2.4 and 2.9, respectively [27].

[38] Hahn and Strassmann, who were studying the decay of U by irradiation with neutrons, discovered fission by identifying the fission fragments, which had been believed to be $_{88}$Ra, $_{89}$Ac, $_{90}$Th, as $_{56}$Ba, $_{57}$La, $_{58}$Ce. Lise Meitner made also a significant contribution to the series of studies as a collaborator of Hahn.

[39] The basic data and theoretical descriptions of fission are given in detail in [27].

[40] As we learn in Chap. 7 many nuclei which undergo spontaneous fission such as actinides to which U belongs are deformed even in their ground states due to the shell effect, i.e., a quantum effect, and the long axis is about 30% longer than the short axis. Also, as shown in Fig. 2.17, most of the fission is an asymmetric fission, where the masses of the two fission fragments are significantly different. Following the original picture of Bohr–Wheeler which is based on the liquid-drop model,

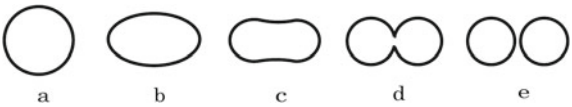


Fig. 2.18 A schematic representation of a symmetric fission

2.3.4.1 The Q-Value of a Spontaneous Fission

Let us first evaluate the Q-value of a spontaneous fission by assuming that a nucleus with a large mass number disintegrates into two fission fragments with equal mass.[41] We have

$$Q \equiv 2B(A/2, Z/2) - B(A, Z) \tag{2.63}$$

$$= A^{2/3} b_{\mathrm{C}} (1 - 2^{-2/3}) \left[\frac{Z^2}{A} - \frac{b_{\mathrm{surf}}}{b_{\mathrm{C}}} \frac{(2^{1/3} - 1)}{(1 - 2^{-2/3})} \right] \tag{2.64}$$

$$\approx A^{2/3} b_{\mathrm{C}} (1 - 2^{-2/3})(Z^2/A - 17.7) \tag{2.65}$$

from the mass formula. Hence, if $Z^2/A > 17.7$, i.e., if $Z > 35$ when we assume $A \sim 2Z$, the nucleus eventually undergoes fission even if we leave it alone. This is called *spontaneous fission*.[42] For example, if one assumes the fission ${}^{236}_{92}\mathrm{U} \rightarrow 2 \times {}^{118}_{46}\mathrm{Pd}$, then the Q-value is about 182 MeV.[43]

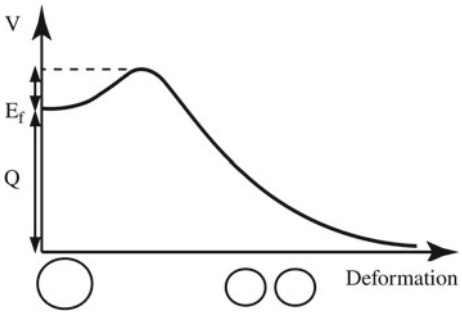


Fig. 2.19 An illustration of the fission barrier by the liquid-drop model

(Footnote 40 continued)
we develop in this book our discussions by assuming that the ground state of nuclei prior to fission, which is a metastable state, is spherical. Incidentally, the shell effect was discovered and the shell model has been established much later.

[41] The heat associated with a nuclear reaction or with an atomic or a molecular reaction is called the Q-value of the reaction. It becomes positive or negative for exothermic or endothermic reactions, respectively. It corresponds to the energy released by fission in the case of a nuclear fission.

[42] Fission is stimulated if the nucleus is irradiated by a photon, or neutron or by other particles. Such reaction is called *induced fission* and is distinguished from the spontaneous fission. It is represented as, for example, (γ,f) and (n,f) for photofission and neutron-induced fission, respectively.

[43] About 200 MeV is a measure of the Q-value for the fission of actinides such as U.

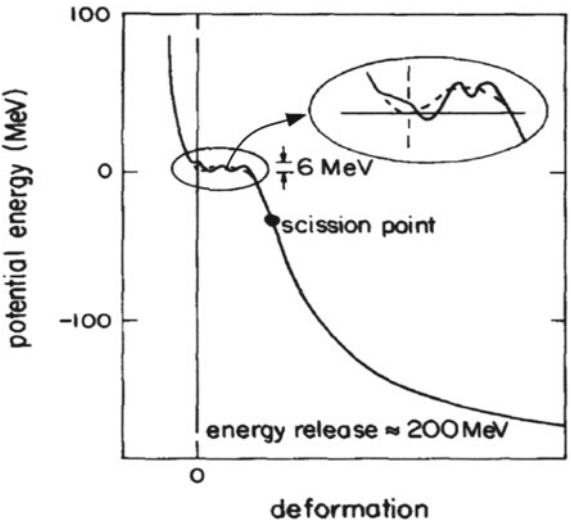


Fig. 2.20 Illustration of the fission barrier by the liquid-drop model with shell effect [27]

The fact that the Q-value is positive does not necessarily mean that fission takes place instantaneously. Figure 2.19 schematically shows the potential barrier governing fission. How to take fission coordinates is itself an important question. Here, we take the nuclear deformation as the fission coordinate corresponding to the conceptual picture for fission shown in Fig. 2.18. This potential barrier has to be overcome by a quantum tunneling in order for fission to occur.[44] Consequently, the lifetime for fission is extremely long. For example, the half-life is $T_{1/2}^{\mathrm{sf}} \sim 10^{17}$ years in the case of ^{238}U. On the other hand, heavy nuclei decay also by emitting α particle. As we learn in Sect. 8.1, the α-decay also occurs by a quantum tunneling. In that case, the abscissa of the potential barrier which corresponds to Fig. 2.19 is the relative coordinate between the α particle and the remaining nucleus in the α-decay, called the daughter nucleus.[45] In the case of ^{238}U, the half-life of α-decay is $T_{1/2}^{\alpha} \sim 10^{9}$ years. As is clear in the WKB formula for a quantum tunneling Eqs. (8.6), (8.7) or a revised formula in the uniform approximation Eq. (2.77), the tunneling probability dramatically decreases following the exponential law as the mass parameter μ of the decaying particle or of the decaying degree of freedom gets large. The μ is nearly equal to the mass of the α particle in the case of α-decay, while the reduced mass of the fission fragments gives a rough measure of μ in the case of fission if the relative coordinate between fission fragments is used as the fission coordinate. Obviously, the

[44] In reality, fission is a quantum tunneling in a multidimensional space with many degrees of freedom.

[45] In the case of α-decay, the potential barrier to be transmitted by a quantum tunneling is located outside the sum of the radii of the α particle and the daughter nucleus. In other words, if we consider the α-decay as a kind of fission process, then the potential barrier appears outside the scission point. That is the reason why the coordinate for the α-decay can be taken to be the coordinate of the relative motion.

latter is much larger. In addition, roughly speaking, the barrier height is proportional to the product of the charges of the fission fragments. One can therefore expect that the barrier height to be transmitted is much higher for fission. It is why the half-life for fission is much longer than that for α-decay. Consequently, the decay of heavy elements occurs mainly by α-decay.

Figure 2.20 shows schematic potential surfaces for fission by Nix. The solid and the dotted lines are the potential surfaces with and without shell correction, which will be discussed later, respectively. It should be remarked that the shell correction introduces a dip in the potential surface at the barrier region.

2.3.4.2 Potential Barrier with Respect to Symmetric Spontaneous Fission and the Fissility Parameter

(1) Fission Coordinate: Deformation Parameter Let us next study how the potential surface with respect to fission shown conceptually in Fig. 2.19 depends on the atomic number and the mass number. Since the isotopes of ^{235,238}U exist in nature with finite but long lifetimes, one can expect that the potential surface for fission has a potential barrier as depicted in Fig. 2.19 up to at least $Z = 92$. On the other hand, there exist no stable nuclei with an extremely large atomic number. One can therefore also expect that the potential barrier ultimately disappears for large enough atomic number. How large is the atomic number at the border?

As stated before, it is not clear at all how to choose the coordinates or parameters for fission. It will be natural to use the distance between two fission fragments as the fission coordinate once they are more apart than the scission point in the late stage of fission. However, the deformation parameters introduced in the following will be more natural to describe the initial stage of fission.

Let us consider fission as a process, where the deformation of a nucleus grows with axial symmetry. The radius $R(\theta)$ of an axial-symmetrically deformed nucleus can be expanded as

$$R(\theta) = R_0 \left[1 + \alpha_0 + \sum_{\lambda=2,4,\ldots} \alpha_\lambda P_\lambda(\cos\theta) \right] \tag{2.66}$$

by using the Legendre functions $P_\lambda(\cos\theta)$, which form a complete set. Here, α_λ are called the deformation parameters. Among them, α_2, α_4 are named quadrupole and hexadecapole deformation parameters, respectively.[46] α_0 is given as a function of $\alpha_{\lambda\neq 0}$ from the condition of volume conservation by considering nucleus as an incompressible liquid. Let us truncate the expansion in Eq. (2.66) by the $\lambda = 2$ term in order to understand the physical meaning of the deformation parameter. If we let the radius for $\theta = 0$ and $\theta = \pi/2$ to be a and b, respectively,

[46] We do not consider $\lambda = 1$, because it describes the translational motion of the nucleus as a whole. There holds the relationship $\alpha_\lambda = \sqrt{(2\lambda+1)/4\pi}\alpha_{20}$ between the α_λ in this section and the deformation parameters $\alpha_{\lambda\mu}$, which will be introduced in Chap. 7.

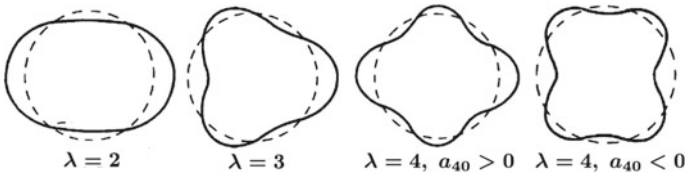


Fig. 2.21 Schematic picture for quadrupole, octupole and hexadecapole deformations

we obtain $a \equiv R(0) = R_0(1+\alpha_2)$, $b \equiv R(\pi/2) = R_0(1-\alpha_2/2) \sim R_0/\sqrt{1+\alpha_2}$ by using $P_2(\cos\theta) = (3\cos^2\theta - 1)/2$. One can see that one obtains a nuclear shape which is elongated (shrunk) along the symmetry axis for positive (negative) α_2. Also, as the expressions for a and b show, the volume is conserved for small deformation in accord with the property of a nucleus as an incompressible liquid. In Eq. (2.66), we assumed the symmetric fission, i.e., the reflection symmetry with respect to the plane which equally divides the symmetry axis. Correspondingly, the deformation parameters of odd order such as the octupole deformation $\lambda = 3$ have been omitted. In Fig. 2.21, we show the nuclear shape corresponding to $\lambda = 2, 3$ and 4.

Exercise 2.13 Confirm that the relation shown in Fig. 2.21 between the nuclear shape and the sign of $\alpha_4 = \sqrt{9/4\pi}\alpha_{40}$ in the presence of hexadecapole deformation holds by using the explicit functional form of the Legendre polynomial $P_4(z)$, $P_4(z) = (35z^4 - 30z^2 + 3)/8$.

(2) Stability with Respect to Fission: Fissility Parameter Both the surface energy $E_{\rm surf}$ and the Coulomb energy $E_{\rm C}$ change when a nucleus changes its shape. Hence it is necessary to study how they depend on the deformation parameters in order to evaluate the potential barrier with respect to fission. The following formulae can be obtained from the mass formula:

$$E_{\rm surf} = b_{\rm surf} A^{2/3}\left[1 + \frac{2}{5}\alpha_2^2 + \frac{5}{7}\alpha_3^2 + \sum_{n\geq 4}\frac{(n-1)(n+2)}{2(2n+1)}\alpha_n^2\right], \tag{2.67}$$

$$E_{\rm C} = b_{\rm C}\frac{Z^2}{A^{1/3}}\left[1 - \frac{1}{5}\alpha_2^2 - \frac{10}{49}\alpha_3^2 - \sum_{n\geq 4}\frac{5(n-1)}{(2n+1)^2}\alpha_n^2\right]. \tag{2.68}$$

If we consider within the framework of the quadrupole deformation and keep terms only up to the second order of the deformation parameter, the change of the energy by deformation is given by

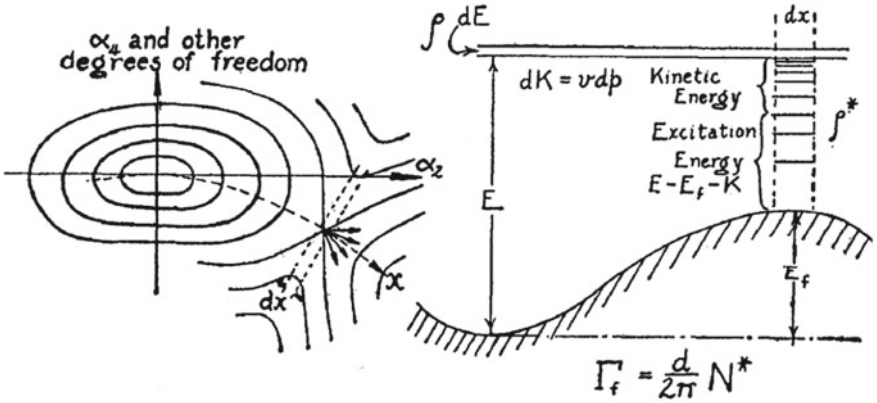


Fig. 2.22 A schematic illustration of the multi-dimensional potential surface for fission and the potential barrier. After [29]

$$\Delta E = \frac{1}{5} b_{\mathrm{C}} \alpha_2^2 A^{2/3} \left(\frac{Z^2}{A}\right)_{\mathrm{cr}} (1 - \chi)\,, \tag{2.69}$$

$$\left(\frac{Z^2}{A}\right)_{\mathrm{cr}} = 2 \times \frac{b_{\mathrm{surf}}}{b_{\mathrm{C}}} \sim 50.3\,, \tag{2.70}$$

$$\chi \equiv \left(\frac{Z^2}{A}\right) \Big/ \left(\frac{Z^2}{A}\right)_{\mathrm{cr}}. \tag{2.71}$$

We see that there appears a potential barrier for the nuclei with $\chi < 1$ and they become metastable with respect to fission. On the contrary, nuclei with a large atomic number for which $\chi > 1$ have no potential barrier and immediately disintegrate by fission.[47] The χ is called the *fissility parameter*.

(3) The Height of the Fission Barrier In reality, the spontaneous fission is a quantum tunneling in a multidimensional space specified either by various deformation parameters or by appropriately chosen coordinates. Figure 2.22, which has been quoted from a paper by Bohr and Wheeler, schematically illustrates fission. The lines in the figure on the left side represent equipotential surfaces. In a simplified picture, one considers that a spherical metastable state decays along a path going through the *saddle point*. Let us define the height of the fission barrier as the height of the saddle point measured from the potential minimum corresponding to the metastable state for fission, and denote it by E_f. The value of E_f can be approximately written down as a function of χ if the fissility parameter χ is small or close to 1. An important point in doing so is that the position of the saddle point moves from a configuration

[47] The critical nucleus is $(A_{\mathrm{cr}},\ Z_{\mathrm{cr}}) \sim (340, 131)$ if we use $N \sim 1.6Z$. However, in more refined estimates which go beyond the quadrupole deformation we used here the potential barrier by the liquid-drop model almost disappears when the atomic number exceeds the critical value $Z_{\mathrm{cr}} \sim 100$ [30].

with small deformation near a in Fig. 2.18 to a configuration near the scission point d as the fissility parameter gets smaller starting from 1. If we take a simplification that the scission point coincides with the saddle point when $\chi = 0$, E_f can be estimated as

$$E_f = 2b_{\rm surf}\left(\frac{A}{2}\right)^{2/3} - b_{\rm surf}A^{2/3} + 2b_{\rm C}\left(\frac{Z}{2}\right)^2 \Big/ \left(\frac{A}{2}\right)^{1/3} + \frac{5}{3}b_{\rm C}\left(\frac{Z}{2}\right)^2 \Big/ 2\left(\frac{A}{2}\right)^{1/3} - b_{\rm C}Z^2/A^{1/3}\,. \tag{2.72}$$

By taking the ratio to the surface energy, we have

$$\begin{aligned}\frac{E_f}{E_{\rm surf}} &\equiv f(\chi)\\ &= (2^{1/3}-1) + \left(2^{1/3} + \frac{5}{3}\frac{1}{2\times 2^{2/3}} - 2\right)\chi\\ &\approx 0.260 - 0.215\chi\,.\end{aligned} \tag{2.73}$$

On the contrary, the saddle point appears in the region of small deformation when χ is close to 1. Hence it makes sense to express the energy surface in the expansion with respect to deformation parameters. It is, of course, needed to include terms beyond the second order in order to determine the position and the height of the saddle point. By keeping up to the fourth order with respect to α_2 and second order concerning α_4, we have

$$\begin{aligned}\Delta E_{{\rm surf}+C} = {} & b_{\rm surf}A^{2/3}\left(\frac{2}{5}\alpha_2^2 + \frac{116}{105}\alpha_2^3 + \frac{101}{35}\alpha_2^4 + \frac{2}{35}\alpha_2^2\alpha_4 + \alpha_4^2\right)\\ & - b_{\rm C}\frac{Z^2}{A^{1/3}}\left(\frac{1}{5}\alpha_2^2 + \frac{64}{105}\alpha_2^3 + \frac{58}{35}\alpha_2^4 + \frac{8}{35}\alpha_2^2\alpha_4 + \frac{5}{27}\alpha_4^2\right)\,.\end{aligned} \tag{2.74}$$

If we determine α_4 for a given α_2 by a variational principle, we obtain

$$\alpha_4 = -\frac{243}{595}\alpha_2^2\,, \tag{2.75}$$

since there exists a coupling term between α_2 and α_4. In consequence, when χ is close to 1, the height of the potential barrier is given by

$$\frac{E_f}{E_{\rm surf}} \equiv f(\chi) = \frac{98}{135}(1-\chi)^3 - \frac{11368}{34425}(1-\chi)^4 + \cdots\,, \tag{2.76}$$

in units of the surface energy.

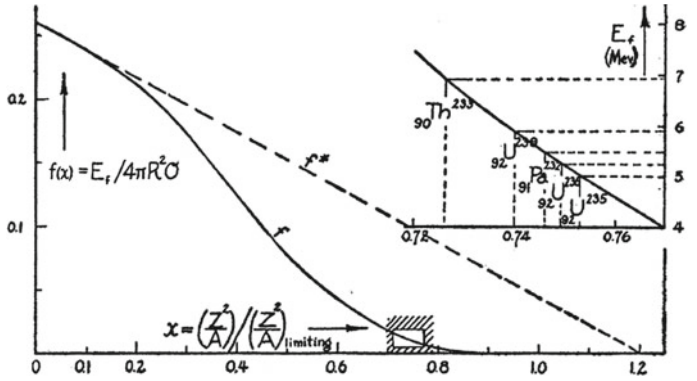


Fig. 2.23 The fissility parameter dependence of the height of the fission barrier plotted as the ratio to the surface energy. After [29]

Figure 2.23 shows the behaviour of $f(\chi)$ after the paper by Bohr and Wheeler [29]. A line which interpolates Eqs. (2.73) and (2.76) is shown as $f(\chi)$. The $f^*(\chi)$ represents $f(\chi)$ given by Eq. (2.73). The value of E_f which is expected when the surface energy for the shaded region around $\chi \sim 0.75$ is set to 530 MeV is shown in the inset on the right corner, since the surface energy does not so change in that region.[48]

The experimental value of E_f can be deduced, for example, from the excitation function of (n,f), (t,pf), (t,df), (d,pf), (γ,f) reactions which are induced by bombarding a target nucleus with either light nuclei or photons.[49] As an example, Fig. 2.24 shows the excitation functions of the fission probabilities for the ^{239}U(n,f) and for the ^{239}U(d,pf) reactions. They are denoted by the solid line and the dots, respectively. Both fission excitation functions exhibit a characteristic threshold rise followed by a flat plateau. A reasonable estimate of the barrier height can be obtained by identifying it to the energy at which the fission probability becomes 1/2 of its plateau value. It is because the tunneling probability or the barrier transmission probability becomes $1/2$ when the decay energy E coincides with the height of the fission barrier, as can be seen from the following formula for the barrier transmission probability in the uniform approximation:

$$P_{\mathrm{UA}} = \frac{1}{1 + \exp(2\int_{r_<}^{r_>} \mathrm{d}r\sqrt{2\mu(V(r) - E)}/\hbar)}\,, \tag{2.77}$$

which is valid from below to above the barrier as long as the fission barrier is a quadratic function or can be well approximated by a quadratic function. In Eq. (2.77),

[48] Bohr and Wheeler estimated the value of E_f for the other nuclei by assuming $(Z^2/A)_{\mathrm{cr}}$ to be 47.8 from the experimental data that E_f is about 6 MeV for ^{239}U.

[49] The scattering cross section plotted as a function of the collision energy is called the excitation function.

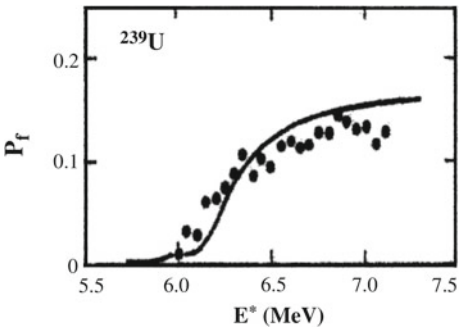


Fig. 2.24 The excitation functions of the induced-fission probabilities of ^{239}U [27]. The *solid line* is for (n,f) and the *dots* are for (d,pf). The abscissa is the excitation energy

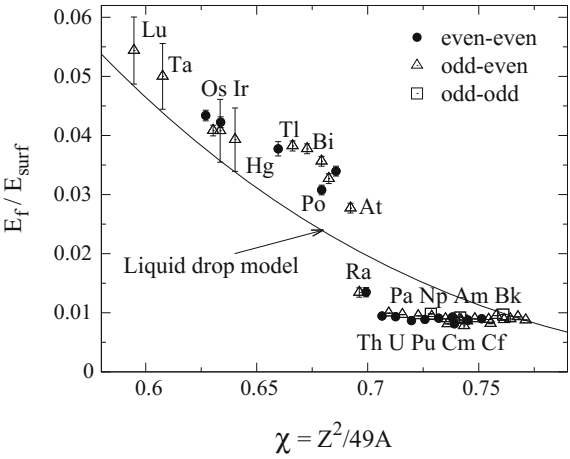


Fig. 2.25 Fission barriers. The data are taken from the compilations in [27]

$r_<$ and $r_>$ are the classical turning points on both sides of the potential barrier: $V(r_<) = V(r_>) = E$, and μ is the reduced mass.[50] The two turning points coincide when the decay energy E matches the height of the fission barrier, so that the resulting barrier transmission probability becomes $1/2$.

Figure 2.25 shows the experimental values of E_f (MeV) in units of the surface energy, which has been assumed to be given by $E_{\rm surf} = 17A^{2/3}$ MeV. The solid line has been calculated by keeping only the first term on the right-hand side of Eq. (2.76). Also, we presented in Table 2.6 the experimental values of $E_f^{\rm exp.}$ together with the predictions by Bohr and Wheeler $E_f^{\rm BW}$ and the binding energy of a neutron $B_{\rm n}^{\rm exp.}$ in the compound nucleus.

What is important in connection with the reactor, which we learn in Sect. 2.3.5, is the sign of $E_f - B_{\rm n}$. If the sign is negative, fission is easily induced even if the energy of the incident neutron is 0. On the other hand, if the sign is positive, an appropriate

[50] In classical mechanics, a particle is reflected at the position where the total energy of the particle becomes identical with the potential energy. Such positions are therefore called *classical turning points* or simply *turning points*.

Table 2.6 The threshold energy for fission E_f and the binding energy of neutron B_n, in units of MeV. The former and the latter are taken from [27, 31], respectively

Nucleus (compound nucleus)	$E_f^{\text{exp.}}$	$B_n^{\text{exp.}}$	$E_f^{\text{exp.}} - B_n^{\text{exp.}}$	E_f^{BW}
^{233}Th	6.4	4.8	1.6	6.9
^{232}Pa	6.3	5.6	0.7	5.5
^{235}U	5.8	5.3	0.5	5.0
^{236}U	5.9	6.5	−0.6	5.25
^{239}U	6.2	4.8	1.4	5.95
^{240}Pu	5.9	6.5	−0.6	

amount of energy has to be supplied in order to induce fission with a large probability. As we learn later, it is the reason why fission can be induced for ^{235}U by a thermal neutron with an extremely small energy, while it is necessary to inject a neutron with the energy of the order of MeV in order to induce fission of ^{238}U. The difference between the two arises from the difference between neutron binding energies in the corresponding compound nuclei, ^{236}U and ^{239}U. Because of the pairing correlation appearing in the mass formula, the B_n for the former is larger by Δ than the value estimated in the simple liquid-drop model without the correction term δ. On the other hand, it gets smaller by Δ in the latter. In fact, the difference between the two $B_n(^{236}\text{U}) - B_n(^{239}\text{U}) = 1.7\,\text{MeV}$ is close to $2\Delta \approx 2 \times \frac{12}{\sqrt{238}} \sim 1.6\,\text{MeV}$.[51]

(4) Spontaneous Fission Half-Lives Figure 2.26 shows the spontaneous fission half-lives $t_{1/2}$ for several actinides (U, Pu, Cm, Cf, Fm) as a function of the fissility parameter χ (filled circles are for even–even nuclei, open circles are for even–odd nuclei. Exactly speaking, the abscissa is slightly different from the χ defined in this book, because a symmetry energy correction is added to the surface energy term in the mass formula). Note that the experimental data lie by and large along a straight line in the semi-logarithmic graph. The detailed structures come from the deviation of the ground state masses from the prediction of the liquid-drop model because of the shell effect. Indeed, if we denote the deviation of the ground state mass from that of the smooth liquid-drop model by δm (MeV), then the values of $\log_{10} t_{1/2}\,(\text{yr}) + 5\delta m$ beautifully align as a function of χ [32] as shown in Fig. 2.27.

The feature shown in Figs. 2.26 and 2.27 can be understood as follows from the point of view of quantum tunneling. Let us denote the curvature of the potential surface for fission in the vicinity of the potential pocket which yields the metastable state by $\omega_0 \equiv (\frac{\partial^2 V}{\partial r^2}/\mu_f)^{1/2}$, where r is an appropriately chosen fission coordinate and μ_f is the corresponding mass parameter. Let us then approximate the potential surface in the vicinity of the potential barrier by a quadratic function with curvature Ω_{fb}. Furthermore, assuming that fission occurs with energy much lower than the

[51] The reactor must have become fairly different from the present one if there existed no pairing correlation between nucleons.

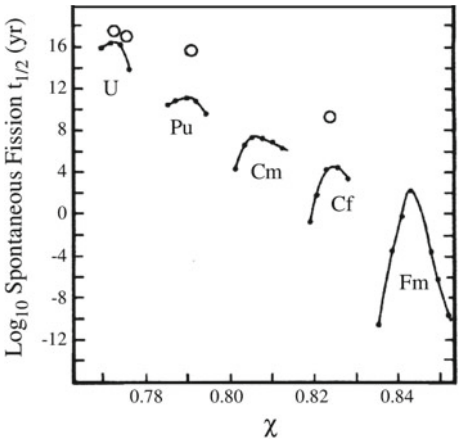


Fig. 2.26 Spontaneous fission half-lives of even–even (*filled circles*) and even–odd (*open circles*) nuclides as a function of the fissility parameter [27]

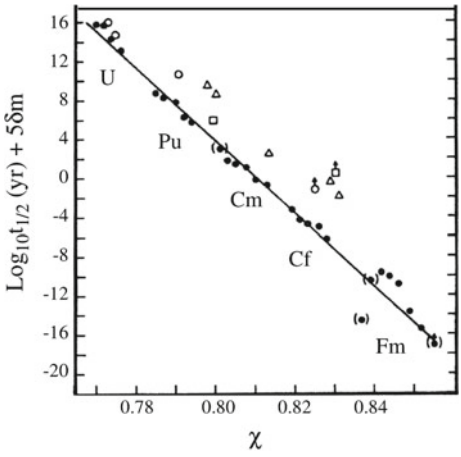


Fig. 2.27 Spontaneous fission half-lives corrected with shell correction [27]

height of the fission barrier, let us represent the tunneling probability in the standard WKB formula by ignoring 1 in the denominator of the formula in the uniform approximation (2.77). The decay width for fission is then given by

$$\Gamma_f = 5 \times \frac{\hbar\omega_0}{2\pi} P_{\text{fis}} \tag{2.78}$$

$$\sim 5 \times \frac{\hbar\omega_0}{2\pi} \exp\left[-\frac{2\pi}{\hbar\Omega_{\text{fb}}}(E_f - E)\right]. \tag{2.79}$$

In Eq. (2.78), following Bohr and Wheeler, we introduced the statistical factor 5 to represent the degeneracy of the quadrupole oscillation which induces fission. Although E_f is given by Eq. (2.76), it will be well represented as $E_f = a - b\chi$ in the linear approximation, since Figs. 2.26 and 2.27 are intended for a narrow region

of χ. Finally, we obtain

$$\log_{10} t_{1/2} \sim A - B\frac{2\pi}{\hbar\Omega_{\rm fb}}\chi \tag{2.80}$$

using two constants A and B. One can thus understand why a linear relationship holds between the fission half-life and the fissility parameter in the semi-logarithmic plot.

Exercise 2.14 Estimate the curvature of the fission barrier $\hbar\Omega_{\rm fb}$ for actinides from Fig. 2.26 or 2.27.[52]

2.3.5 Application to Nuclear Power Generation

The nuclear power generation in operation today exploits the energy release, called *nuclear energy*, due to fission. In this subsection, we learn the principles of reactor and several key words.

2.3.5.1 Nuclear Reactions in Reactor, Principles of Reactor, Chain Reaction, Neutron Moderator, Neutron Absorber

Figure 2.28 illustrates the nuclear reactions induced by injecting a neutron into a mass of uranium which is a mixture of ^{235}U and ^{238}U. ^{235}U disintegrates into two large nuclei with about half the atomic and mass numbers of ^{235}U (see Fig. 2.17), and two to three neutrons on average.

The phenomenon shown in Fig. 2.28 can be understood as follows. As already stated concerning the Q-value for fission, the nuclear energy of around 200 MeV is

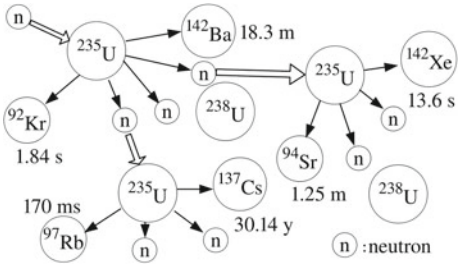


Fig. 2.28 Illustration of nuclear reactions in reactor (*chain reaction*)

[52] The information on both the potential surface and the effective mass is needed in order to theoretically evaluate the fission width. Nowadays, the potential surface can be obtained with relatively high accuracy using, for example, the macroscopic–microscopic method, which refines the liquid-drop model by adding the shell correction and will be described in Sect. 7.6.1. On the contrary, it is difficult to estimate the mass parameter with high reliability. One can hope to obtain important phenomenological information on the effective mass for fission by using the results of this exercise.

released per fission. Though most of the released energy is used as the kinetic energy of the fission fragments, a part of it becomes their excitation energies. Roughly speaking, the fission fragment loses its excitation energy by emitting one neutron if the excitation energy amounts to 8 MeV, which is an average binding energy of nucleon. The resulting nucleus is usually a neutron-rich unstable nucleus, so that it continues to lose its energy by repeating β-decay. Since the β-decay proceeds in obedience to selection rules [33], the resulting daughter nucleus is not necessarily in the ground state, but sometimes is above the threshold energy for neutron emission. In that case, the state decays by emitting a neutron. Since the β-decay usually takes place in the time scale of the order of seconds to minutes, those neutrons emitted after the β-decay are emitted with a time delay compared with the neutrons emitted immediately after fission. Those neutrons are therefore called *delayed neutrons*. In comparison, the neutrons emitted immediately after fission are called *prompt neutrons*. In consequence, two large fragments and two to three neutrons are emitted by the decay of U.[53] The average number of neutrons emitted in the thermal-neutron-induced fission of ^{235}U is 2.47 as stated before, although it fluctuates due to the existence of various decay processes as shown in Fig. 2.17.

The emitted neutrons are absorbed by the surrounding ^{235}U, and successively induce fission leading to a *chain reaction*.[54] It is the principle of reactor to utilize the nuclear energy by appropriately removing the emitted neutrons with an absorber called *control rod* in order to keep the number of thermal neutrons in the space constant, and thus by safely sustaining the chain reaction. A minimum condition is needed for the amount of U fuel in order to sustain the chain reaction, which is called the *critical mass*.

2.3.5.2 The Neutron Absorption Cross Section, Enriched Uranium, and Neutron Moderator

The cross section of the neutron-induced fission of U strongly depends on the isotopes and the energy of the incident neutron. Figure 2.29 shows the neutron-induced fission cross section of ^{235}U and ^{238}U (cited from [33], see also [34]). The figure shows that ^{238}U does not cause fission unless the energy of neutron becomes as high as 1 MeV. This is the reason why no fission of ^{238}U is seen in Fig. 2.28. On the other hand, the energy of thermal neutron 1/40 eV is sufficient to induce fission of ^{235}U. The difference between the threshold energies for the induced fission of ^{235}U and ^{238}U originates from the pairing correlation between nucleons as stated before.

---

[53] Most of the neutrons are the prompt neutrons which are emitted at times shorter than 4×10^{-14} s. Though the ratio of the delayed neutron is small, it plays an important role in controlling nuclear reactors [6, 33, 34].

[54] It is Fermi and his collaborators who succeeded in the chain reaction of the induced fission of U by a slow neutron for the first time, and the experiment was performed at the University of Chicago on December 2, 1942.

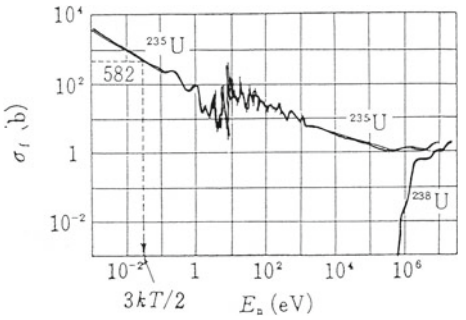


Fig. 2.29 Neutron induced fission cross section [33]

Because of this difference, the *enriched uranium*, which has the composition of ^{235}U with a larger percentage than that of the naturally occurring uranium 0.720%, is used as the fuel for reactors.[55]

Figure 2.29 shows that the induced fission cross section of ^{235}U decreases nearly proportionally to the inverse of the velocity of the incident neutron v as the energy of neutron increases (*1/v-law*). We learn the reason in Sect. 9.3. On the other hand, the energy spectrum of the neutrons emitted in the thermal neutron induced fission of ^{235}U can be well represented as

$$N(E) \propto \sqrt{E}\exp(-E/E_0) \sim \sqrt{E}\exp(-E/1.29\,\mathrm{MeV}) \tag{2.81}$$

using the laboratory energy E, and distributes with its maximum at near $E = E_0/2 \sim 0.65$ MeV. Figure 2.30 shows the laboratory neutron kinetic energy spectrum for thermal neutron-induced fission of ^{235}U. The average energy of the emitted neutrons is $\bar{E} = 1.5E_0 \sim 2$ MeV.[56] Although these fast neutrons can induce fission of ^{238}U, the cross section is much smaller than that of the thermal neutron-induced fission of ^{235}U as Fig. 2.29 shows. Moreover, the induced fission cross section of ^{235}U by high-energy neutrons is small, so that the cross section becomes effectively small. The neutron moderator is therefore introduced in reactors so as to reduce the kinetic energy of neutrons to that of the thermal neutrons.[57]

Exercise 2.15 Summarize why enriched uranium is used for nuclear reactors.

Sidebar: Natural Nuclear Fission Reactor A number of uranium ores, whose isotope ratio of ^{235}U is significantly smaller than the standard value 0.720% in the

[55] In commercial reactors, the enrichment of ^{235}U is typically about 3–4%.

[56] The center of mass energy spectrum of neutrons emitted from a nucleus in the excited state with temperature T is expected to be given by $\varepsilon_n \exp(-\varepsilon_n/T)$, and is well described by the theory called the *evaporation theory*. The dashed line in Fig. 2.30 represents the energy spectrum expected from the evaporation theory transformed to that in the laboratory frame by taking into account the finite velocity of the fission fragment.

[57] The reactor which uses high energy neutrons, instead of neutrons which have been cooled down to thermal neutrons due to the elastic scattering in the neutron moderator, is called *fast reactor* or *fast neutron reactor*.

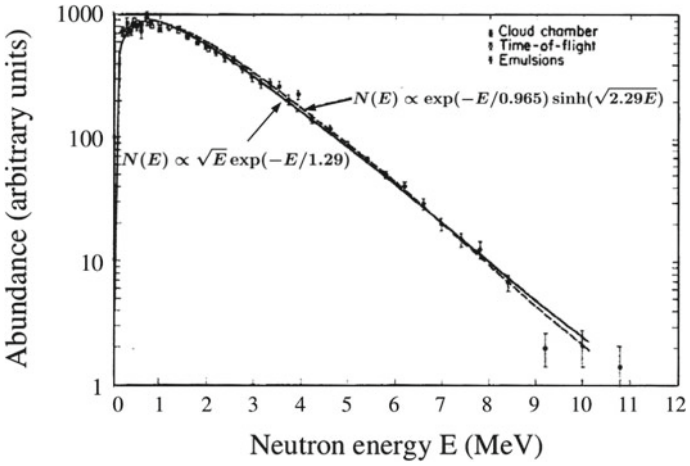


Fig. 2.30 Kinetic energy spectrum of neutrons (Laboratory system) [27]

naturally occurring uranium, have been discovered in the uranium mines at Oklo in Gabon (Gabonese Republic), Africa. This suggests that there has been once natural nuclear fission reactors in the uranium deposits at Oklo.

2.3.5.3 Nuclear Waste Problem: Transmutation

Many of the fission products are radioactive nuclei with finite lifetimes as written in Fig. 2.28. In particular, the relatively long half-lives of $^{137}_{55}$Cs and $^{90}_{38}$Sr are 30.14 and 28.78 years, respectively, which are of the same order as the human life span. In addition, transuranium elements such as $^{237}_{93}$Np, whose half-life exceeds 200 million years, are produced. In the nuclear power industry this is a serious nuisance. These radioactivities cause a biological hazard in discarded nuclear waste for a long time. It is of critical importance to handle these long-lived nuclear wastes, and the studies of nuclear transmutation are going on.

2.3.6 Fission Isomers

At the end of this section, let us learn about *fission isomers*. Figure 2.31 shows the excitation function of the neutron-induced fission of ^{230}Th, i.e., $^{230}_{90}$Th(n,f). Unlike Fig. 2.24, there appears a clear resonance structure with the width of 40 keV at the incident energy of neutron of about 720 keV. Figure 2.32 compares the excitation functions of the $^{230}_{90}$Th(n,f) and $^{230}_{90}$Th(d,pf) reactions, which have been obtained by

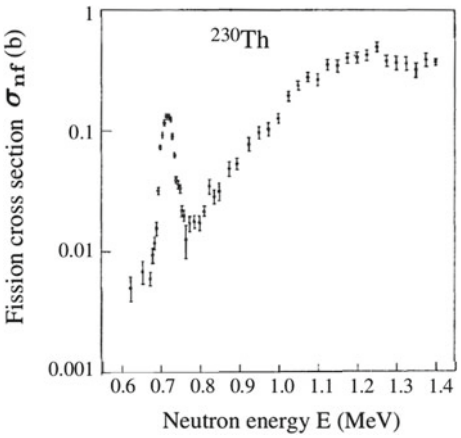


Fig. 2.31 The excitation function of the neutron induced fission of ^{230}Th, showing a resonance. Taken from [35]

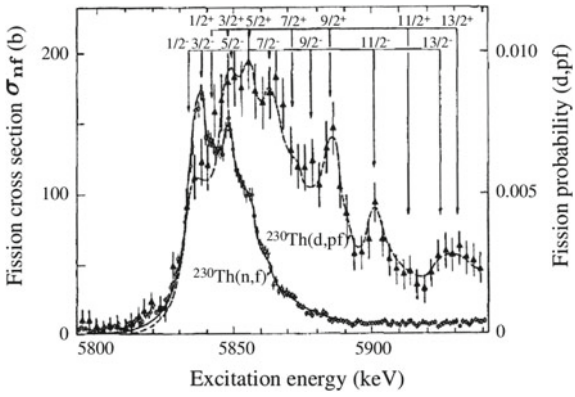


Fig. 2.32 Detailed structure of the excitation function of two induced fissions of ^{230}Th. Taken from [36]

later experiments with high resolution. The abscissa of Fig. 2.32 is the excitation energy of $^{231}_{90}$Th.

The excitation function of fission will be a monotonic function if the potential surface for fission has only a single barrier as predicted by the simple liquid-drop model and as has been shown in Fig. 2.19. In reality, the potential surface has multiple-barriers depending on the nucleus due to the shell correction energy representing the shell effect. The situation is shown in Fig. 2.33. It shows how the understanding for the structure of fission barrier has evolved with time.[58]

The structure seen in Fig. 2.31 was originally interpreted as the meta-stable β-vibrational level produced in the second potential minimum. However, using the fine

[58] One of the powerful methods to obtain the potential surface with multiple-potential barriers is the macroscopic–microscopic method which modifies the liquid-drop model by adding shell correction (see Sect. 7.6.1). In the fission of ^{231}Th, the first fission barrier is lowered by axial asymmetry. The axial symmetry is recovered in the second fission barrier. However, the barrier height gets lower by considering mass asymmetry, and furthermore there appears the third potential minimum.

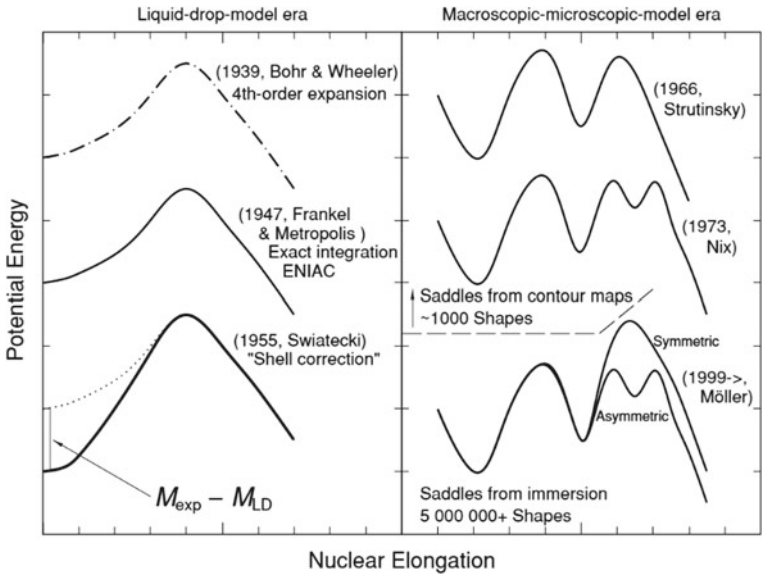


Fig. 2.33 Time evolution of the theory for fission barrier, taken from [37]

structures seen in Fig. 2.32 as the experimental evidence, these structures are now understood to be associated with the rotational motion involving parity doublet, i.e., the positive and negative parity rotational bands, which have almost the same moment of inertia, yielded in the third potential minimum associated with the mass asymmetric fission [36, 38] (see the right-bottom curves in Fig. 2.33). The position, width and spin–parity of each resonance state shown in the figure have been determined by the high-resolution measurement of the excitation function using, for example, the time of flight (TOF), the measurement of the angular distribution of fission fragments, the simultaneous measurements of (n,f) and (d,pf) reactions, and the theoretical analyses by the parity-doublet rotational model. The ratio of the length of the long axis to that of the short axis obtained from the level splitting is 3:1, and matches the deformation at the third potential minimum.[59]

Figure 2.34 shows a few energy levels near the ground state of ^{238}U and metastable states in the second potential well together with their spin and parity. The latter states are called fission isomers.

The fission isomers are a kind of either *superdeformed states*, which we learn in Sect. 7.6.2 and whose ratio of the length of the long axis to that of short axis is about 1.6–1.8, or *hyperdeformed states* which have even larger ratio of the lengths of two axes.[60] As we learn in Chap. 7, a characteristic of deformed states is that there

[59]The ratio of the length of the long axis to that of the short axis is 2:1 for the second potential minimum.

[60]The ratio of the length of the long axis to that of the short axis is about 1.3 for usual deformed nuclei such as the ground state of U. In comparison, the moment of inertia of fission isomers is 2.2

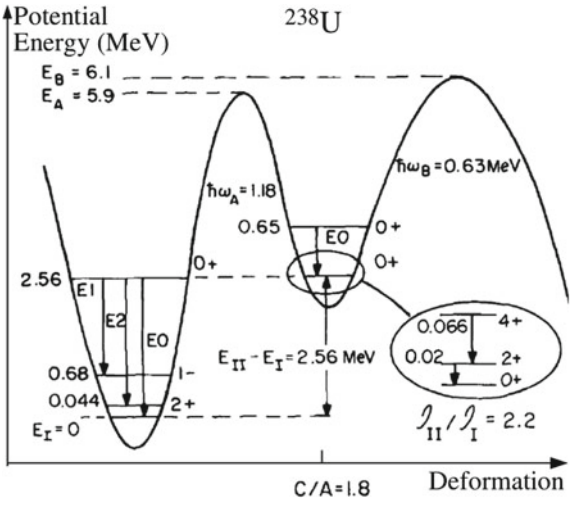


Fig. 2.34 The structure of ^{238}U. Fission isomers. Taken from [39]

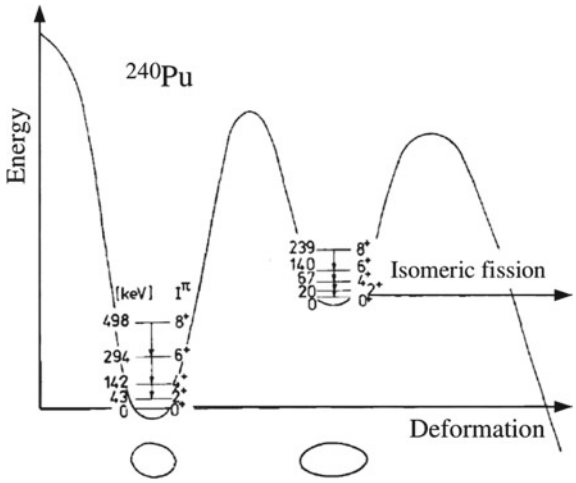


Fig. 2.35 The structure of ^{240}Pu. Fission isomers. Taken from [40]

appear a characteristic group of states called rotational bands. Figure 2.35 compares the rotational bands built on the ground state and on a fission isomer by taking the case of ^{240}Pu as an example. The large difference of the deformation between the two bands can be deduced from the difference of the corresponding level spacing.

(Footnote 60 continued)
times that of the ground state for ^{238}U as shown in Fig. 2.34. ^{8}Be, which has the dumb-bell structure of two touching α particles, has also 2:1 for the ratio of the length of the long axis to that of the short axis, and hence is one of the hyperdeformed states.

References

1. E. Segré, *From X-Rays to Quarks: Modern Physicists and Their Discoveries* (W. H. Freeman and Company, San Francisco, 1980)
2. M. Nogami, *Nuclear Physics*, Japanese edn. (Shoukabou, Tokyo, 1973)
3. T. de Forest Jr., J.D. Walecka, Adv. Phys. **15**, 1 (1966)
4. B. Hahn, D.G. Ravenhall, R. Hofstadter, Phys. Rev. **101**, 1131 (1956)
5. A. Tamii et al., Phys. Rev. Lett. **107**, 062502 (2011)
6. W.N. Cottingham, D.A. Greenwood, *An Introduction to Nuclear Physics*, 2nd edn. (Cambridge University Press, Cambridge, 2001)
7. R. Hofstadter, F. Bumiller, M.R. Yearian, Rev. Mod. Phys. **30**, 482 (1958)
8. N. Takigawa, M. Ueda, M. Kuratani, H. Sagawa, Phys. Lett. B **288**, 244 (1992)
9. J.S. Al-Khalili, J.A. Tostevin, Phys. Rev. Lett. **76**, 3903 (1996)
10. B. Abu-Ibrahim, Y. Suzuki, Phys. Rev. C **61**, 051601 (2000)
11. J. Kasagi, H. Yuki, T. Baba, T. Noda, T. Ohtsuki, A.G. Lipson, J. Phys. Soc. Jpn. **71**, 2881 (2002)
12. Y. Kato, N. Takigawa, Phys. Rev. C **76**, 014615 (2007). And references therein
13. G. Audi, A.H. Wapstra, C. Thibault, Nucl. Phys. A **729**, 337 (2003)
14. R. Shurtleff, E. Derringh, Am. J. Phys. **57**, 552 (1989)
15. T. Arima, Master thesis, Tohoku University
16. W.-M. Yao et al. (Particle Data Group), J. Phys. G 33, 1 (2006)
17. L. Alvarez et al., Phys. Rev. **105**, 1127 (1957)
18. S.E. Jones, Nature **321**, 127 (1986)
19. K. Ikeda, N. Takigawa, H. Horiuchi, Prog. Theor. Phys. Suppl. **E68**, 464 (1968)
20. K. Ikeda, T. Marumori, R. Tamagaki, H. Tanaka, J. Hiura, H. Horiuchi, Y. Suzuki, F. Nemoto, H. Bando, Y. Abe, N. Takigawa, M. Kamimura, K. Takada, Y. Akaishi, S. Nagata, Prog. Theor. Phys. Suppl. **52** (1972); K. Ikeda, R. Tamagaki, S. Saito, H. Horiuchi, A. Tohsaki-Suzuki, M. Kamimura, Prog. Theor. Phys. Suppl. **62** (1977)
21. H. Horiuchi, K. Ikeda, K. Kato, Prog. Theor. Phys. Suppl. **192**, 1 (2012)
22. C.M. Lederer, V. Shirley, *Table of Isotopes*, 7th edn. (Wiley, New York, 1978)
23. N. Takigawa, A. Arima, Nucl. Phys. A **168**, 593 (1971)
24. P. Möller, J.R. Nix, W.D. Myers, W.J. Swiatecki, At Data Nucl. Tables **59**, 185 (1995); P. Möller, J.R. Nix, Nucl. Phys. A **536**, 20 (1992); H. Koura, M. Uno, T. Tachibana, M. Yamada, Nucl. Phys. A **674**, 47 (2000); H. Koura, T. Tachibana, M. Uno, M. Yamada. Prog. Theor. Phys. **113**, 305 (2005)
25. S. Yusa, private communication
26. K.F. Flynn, L.E. Glendenin, ANL-7749 (1970); cited in [27]
27. R. Vandenbosch, J.R. Huizenga, *Nuclear Fission* (Academic Press, New York, 1973)
28. O. Hahn, F. Strassmann, Naturwiss. **27**, 11 (1939)
29. N. Bohr, J.A. Wheeler, Phys. Rev. **56**, 426 (1939)
30. F. Ivanyuk, K. Pomorski, Phys. Rev. C **79**, 054327 (2009); Int. J. Mod. Phys. E **19**, 514 (2010)
31. A.H. Wapstra, G. Audi, Nucl. Phys. A **432**, 1 (1985)
32. W.J. Swiatecki, Phys. Rev. **100**, 937 (1955)
33. K. Yagi, *Nuclear Physics*, Japanese edn. (Asakura, Tokyo, 1971)
34. W.S.C. Williams, *Nuclear and Particle Physics* (Clarendon press, Oxford, 1991)
35. G.D. James, J.E. Lynn, L.G. Earwaker, Nucl. Phys. A **189**, 225 (1972)
36. J. Blons, Nucl. Phys. A **502**, 121c (1989)
37. P. Möller, A.J. Sierk, T. Ichikawa, A. Iwamoto, R. Bengtsson, H. Uhrenholt, S. Åberg, Phys. Rev. C **79**, 064304 (2009)
38. P. Möller, J.R. Nix, in *Proceedings of the Third IAEA Symposium on the Physics and Chemistry of Fission, Rochester, 1973*, Vol. I (International Atomic Energy Agency, Vienna, 1974), p. 103
39. R. Vandenbosch, Nucl. Phys. A **502**, 1c (1989)
40. V. Metag, D. Habs, H.J. Specht, Phys. Rep. **65**, 1 (1980); The original paper is H.J. Specht, J. Weber, E. Konecny, D. Heunemann. Phys. Lett. B **41**, 43 (1972)

http://www.springer.com/978-4-431-55377-9

Fundamentals of Nuclear Physics

Takigawa, N.; Washiyama, K.

2017, XV, 269 p. 86 illus., 6 illus. in color., Hardcover
ISBN: 978-4-431-55377-9